Protracted magmatism and crust–mantle interaction during continental collision: insights from the Variscan granitoids of the external western Alps

Kévin Fréville, Jean-Baptiste Jacob, Jonas Vanardois, Pierre Trap, Jérémie Melleton, Michel Faure, Stephane Guillot, Emilie Janots, Olivier Bruguier, Marc Poujol, et al.

International Journal of Earth Sciences
https://doi.org/10.1007/s00531-024-02420-y

ORIGINAL PAPER

Protracted magmatism and crust–mantle interaction during continental collision: insights from the Variscan granitoids of the external western Alps

Kévin Fréville[1,2] · Jean-Baptiste Jacob[3,4] · Jonas Vanardois[5,6] · Pierre Trap[6] · Jérémie Melleton[2] · Michel Faure[1] · Stéphane Guillot[4] · Emilie Janots[4] · Olivier Bruguier[7] · Marc Poujol[8] · Philippe Lach[2] · Sidonie Révillon[9]

Received: 11 October 2023 / Accepted: 17 April 2024

Abstract

Variscan granitoids and associated mafic rocks exposed in the External Crystalline Massifs (ECM) of the Western Alps document the Variscan stages from the early Carboniferous collision to the early Permian post-collisional setting. Our study focuses on the Central part of the ECM, synthesizing newly acquired and existing geochronological, whole-rock geochemical and isotopic data. We identified two distinctive magmatic series: (i) high-K calc-alkaline granitoids, which range from magnesian (MgG) to ferro-magnesian (FeMgG) rocks; (ii) ultra-high-K metaluminous (UHKM) rocks ("durbachites"). These series were emplaced roughly simultaneously between ca. 350 and 300 Ma, with two main episodes during the Visean (ca. 348–335 Ma) and the late Carboniferous (305–299 Ma), with a more limited activity in between. A younger Permian event at ca. 280–275 Ma has also been identified in one granitoid pluton. Contemporaneous emplacement of these two series reflects concomitant crustal anatexis and melting of LILE–LREE-rich metasomatized lithospheric mantle. Trace elements and Nd–Sr isotopes reveal significant hybridization between these two magmatic end members, by magma mixing, or assimilation of crystallized mafic ultrapotassic enclaves in the high-K calc-alkaline granitoids. Granitoid composition evolves over time, especially SiO_2, Mg#, Sr/Y, La/Yb and Nb/Ta, possibly explained by increasing differentiation of magmas over time, changes in the crust versus mantle sources mass-balance, and decrease in melting pressure due to the orogenic collapse. The εNd_i values of both high-K calc-alkaline granitoids and durbachites decreases from [−3.8; −2.9] to [−6.4; −5.2] between 345 and 320 Ma, possibly indicating an increasing influence of subducted/relaminated crustal material contaminating the lithospheric mantle source. εNd_i values then rise to [−3.7; −0.5] during the late Carboniferous, possibly due to progressive exhaustion of the enriched mantle source, or advection of the asthenosphere during the post-collisional stage.

Keywords Variscan belt · Orogenic granitoids · Mg–K magmatism · LA-ICPMS zircon dating

✉ Jean-Baptiste Jacob
j.b.jacob@mn.uio.no

[1] UMR 7327, Institut des Sciences de la Terre d'Orléans, Université d'Orléans, CNRS, 45071 Orléans Cedex 2, France

[2] BRGM-French Geological Survey, 3 Avenue Claude Guillemin, 45100 Orléans, France

[3] The Njord Centre, Department of Geosciences, University of Oslo, Oslo, Norway

[4] Univ. Grenoble Alpes, Univ. Savoie Mont Blanc, CNRS, IRD, Univ. Gustave Eiffel, ISTerre, 38000 Grenoble, France

[5] UMR 7063, Ecole et Observatoire des Sciences de la Terre, Université de Strasbourg, 67084 Strasbourg Cedex, France

[6] UMR 6249 Chrono-environnement, Université de Franche-Comté, 16 route de Gray, 25030 Besançon Cedex, France

[7] Géosciences Montpellier, UMR 5243, Université de Montpellier, Place Eugène Bataillon, 34095 Montpellier Cedex 5, France

[8] Univ. Rennes, CNRS, Géosciences Rennes – UMR 6118, Rennes, France

[9] Sedisor, Place Copernic, 29280 Plouzane, France

Published online: 13 June 2024

Introduction

Collisional belts can be the site of intense magmatic activity, in particular in response to thermal relaxation and gravitational collapse of the thickened lithosphere. Large granitoid batholiths and migmatite domes are commonly formed during syn- to late-collisional stages (Finger et al. 1997; Moyen et al. 2021; Pitcher 1987; Teyssier and Whitney 2002), by the accumulation of multiple batches of magma emplaced over millions to tens of million years (Clemens 2012; Laurent et al. 2017; Schaltegger et al. 2019).

The Paleozoic Variscan Belt of Western and Central Europe has been for long an important site for studying magmatic processes in collisional orogens (Didier et al. 1982; Finger et al. 1997; Pitcher 1987). Recent efforts aimed to build a coherent geodynamic framework integrating tectonic–metamorphic and magmatic evolution, shedding light on the interplay between crustal and mantle processes during the Variscan Orogeny (Hora et al. 2021; Laurent et al. 2017; Martínez Catalán et al. 2021; Moyen et al. 2017; Vanderhaeghe et al. 2020; Žák et al. 2014). However, many of these studies have been focused on large Paleozoic massifs like the French Massif Central or the Bohemian Massif, where the largest Variscan batholiths are exposed (Ledru et al. 2001; Žák et al. 2014). Peripheral and smaller Paleozoic massifs have been comparatively overlooked, especially in the eastern domain due to the Alpine overprint. The Western Alps provide a well-exposed crustal section from the upper to the partially molten middle–lower crust in the External Crystalline Massifs (ECM), which contain numerous granitoid intrusions emplaced at different structural levels (Fig. 1), and with little impact of Alpine metamorphism.

Based on scarce geochronological data, Debon and Lemmet (1999) suggested that the ECM granitoids were emplaced in two magmatic episodes during the syn- and post-collisional stages at ca. 340 and 305 Ma. However, this model has been questioned by a recent geochronological study of the Aar Batholith (Ruiz et al. 2022), the northernmost Variscan plutonic formation in the ECM (Fig. 1). The Aar Batholith study identified multiple episodes of magmatic emplacement during the Carboniferous, challenging the previously suggested timing. Consequently, further investigation is needed to clarify the timing of magmatic activity and the relationship between granite emplacement and regional tectono-metamorphic evolution in the less-studied central ECM of Belledonne, Grande-Rousses and Pelvoux.

Another interesting feature of the ECM granitoids is their close association with a set of mafic to intermediate, Mg-rich (ultra)-potassic monzodiorite to quartz syenite and lamprophyres akin to the durbachite suite (Von Raumer et al. 2014). They are volumetrically minor but spatially widespread in the ECM basement (Banzet 1987; De Boisset 1986; Debon et al. 1998; Schaltegger 1997). Similar rocks in other Variscan massifs have been interpreted as markers of the contribution of a metasomatized mantle source to the Variscan magmatism (Hora et al. 2021; Janoušek and Holub 2007; Laurent et al. 2017; Soder and Romer 2018). Variation in geochemical and isotopic compositions of these series over space and time offer crucial insights into mantle heterogeneities and compositional evolution during the Variscan collision.

We compiled existing literature data and collected samples from various granitoid and mafic/intermediate plutons representative of the lithological diversity of the ECM in the Belledonne–Pelvoux area. Our new dataset, including zircon U–Pb ages, whole-rock major-, trace-element and Sr–Nd isotopic data on 22 samples, aims to constrain the timing of syn- to late-collisional magmatism in the ECM, establish the link between granite emplacement and regional tectono-metamorphic evolution and examine the geochemical and isotopic evolution of magmatism over time.

Geological setting

The ECM, representing the exposed portions of the Variscan basement in the external Western Alps (Fig. 1a), comprise a heterogeneous metamorphic pile predominantly consisting of Cambrian–Ordovician mafic to felsic igneous and sedimentary protoliths. These rocks underwent greenschist- to granulite-facies metamorphism during the Variscan collision (Bussy et al. 2011; Fréville et al. 2022 2018; Guillot and Ménot 2009; Jacob et al. 2021a, 2022). This metamorphic pre-Variscan basement was intruded by numerous Carboniferous granitoid plutons, and the entire complex is overlain by late-Carboniferous and Mesozoic sedimentary rocks (Fig. 1b). Alpine Orogeny affected the Variscan basement, with localized deformation along brittle–ductile shear zones associated with low-grade metamorphism (250–350 °C and 0.1–0.5 GPa, Bellanger et al. 2015).

In the Belledonne, Grandes-Rousses and Pelvoux Massifs, there is a gradual increase of Variscan metamorphic conditions from West to East. The western units consist of metasedimentary series forming the "Série Satinée" (Bordet and Bordet 1963, Fig. 2) metamorphosed at greenschist to low-T amphibolite-facies conditions (Fréville et al. 2018; Ménot 1988). Eastward, peak-T metamorphic conditions increase gradually (Guillot and Menot 1999) and reach granulite-facies conditions in central and eastern Pelvoux (> 800 °C; Fréville et al. 2022; Grandjean et al. 1996; Jacob et al. 2022), where both mafic and felsic protoliths were intensely migmatized (Barféty and Pêcher 1984; Le Fort

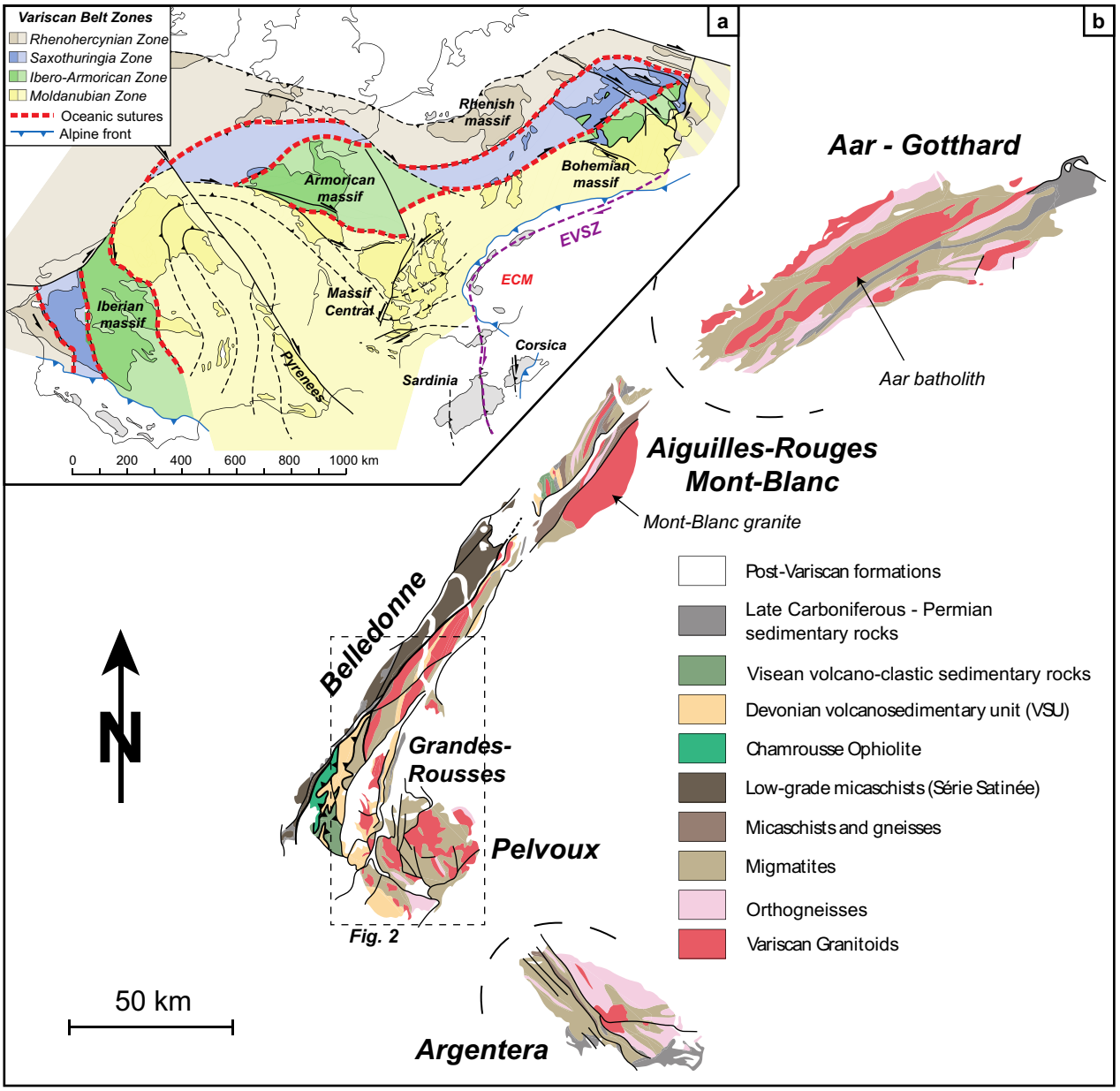

Fig. 1 **a** Location of the External Crystalline Massifs (ECM) within the Variscan framework, modified after Franke et al. (2017). **b** Simplified geological map of the ECM. Dashed rectangle shows the extent of Fig. 2

1971; Pecher 1970). These migmatitic series contain relics of retrogressed eclogites and high-pressure (HP) granulites marking an early collisional HP stage (ca. 1.4–1.8 GPa, 650–730 °C) during the Visean (ca. 340–330 Ma; Jacob et al. 2021a, 2022). In southern Belledonne and western Pelvoux, pre-Variscan bimodal acid–basic magmatic series and volcano-clastic series, presumably of late Devonian to early Carboniferous age (ca. 370–350 Ma), are metamorphosed under the amphibolite-facies conditions (Fréville et al. 2018, 2022; Ménot 1986; Ménot et al. 1987).

Variscan tectonics in the ECM involved three deformation stages. The first event (D1), occurring during the early Carboniferous (350–330 Ma), involved east-directed nappe stacking (in present-day reference frame), primarily observed in the SW Belledonne Massif, resulting in a shallow dipping S1 foliation (Fig. 3a) (Fernandez et al. 2002; Fréville et al. 2018). The D1 event induced crustal thickening, leading to HP granulitic–eclogitic metamorphic conditions at the base of the nappe pile, with localized partial melting at deeper structural levels (Fréville

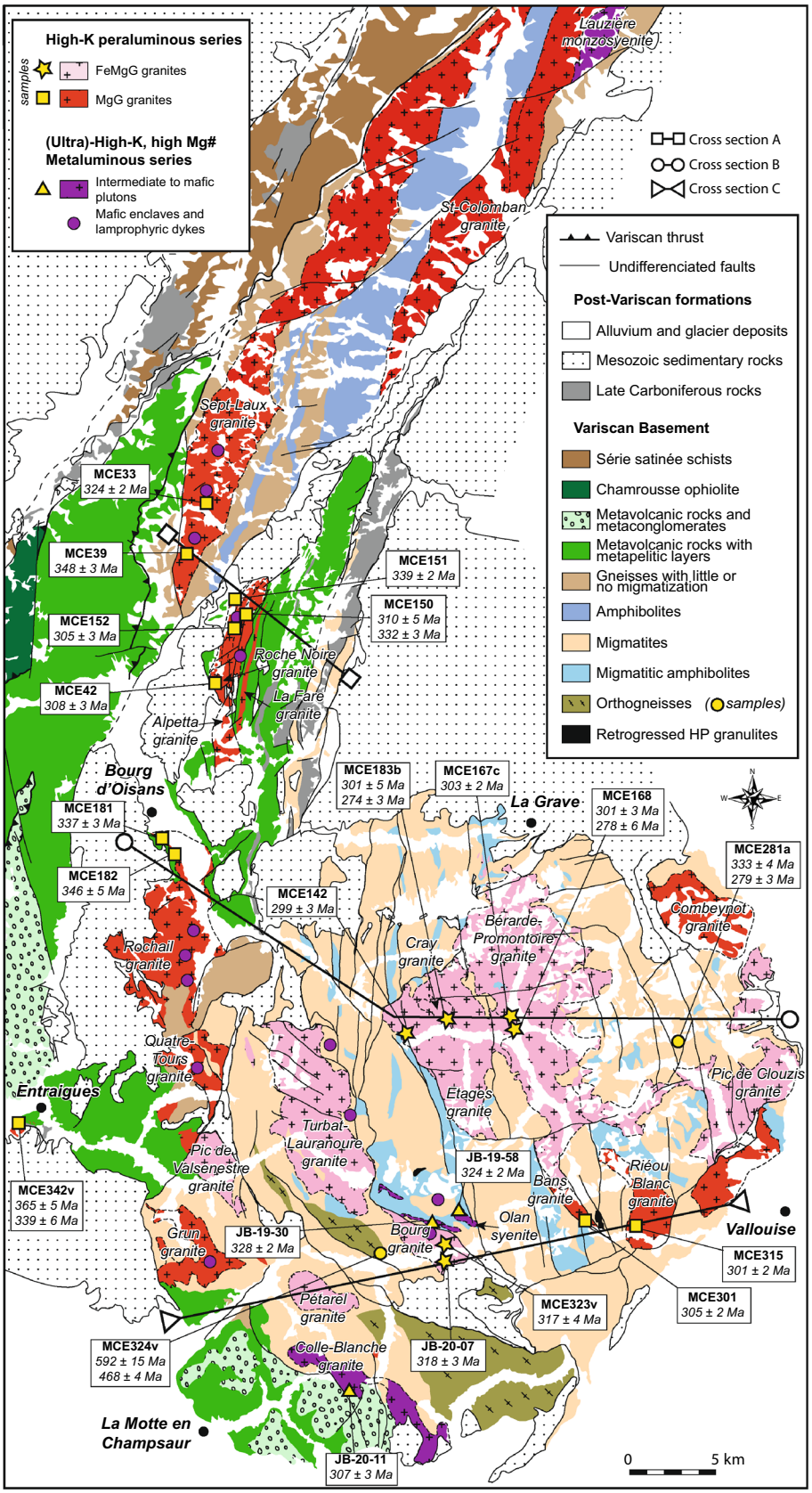

Fig. 2 Simplified geological map of the Pelvoux and Grandes-Rousses massifs and a part of the Belledonne Massif showing the location of the dated samples. Modified after Fréville et al. (2018)

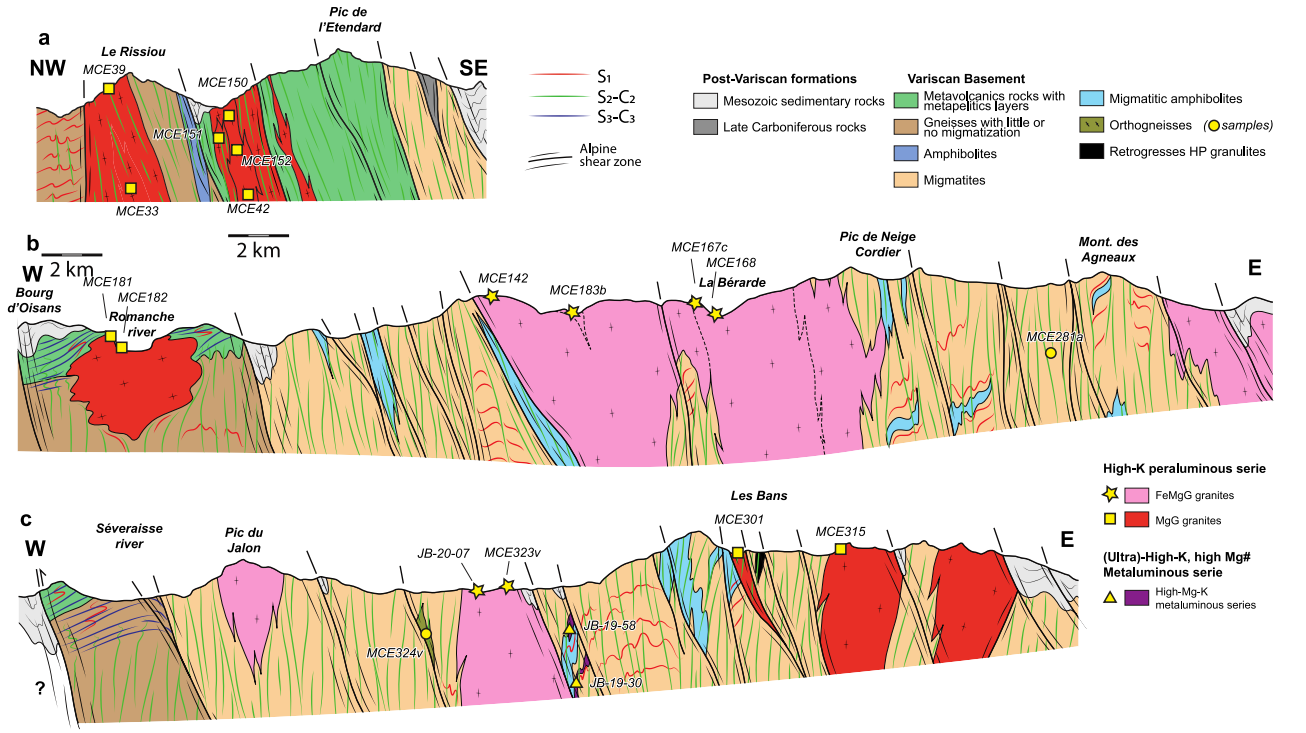

Fig. 3 **a** The NW–SE cross section through the Grandes-Rousses Massif and a part of the Belledonne Massif. **b** The NW–SE cross section through the northern part of the Pelvoux Massif. **c** The W–E cross section through the center part of the Pelvoux Massif

et al. 2018, 2022; Jacob et al. 2021a; Vanardois et al. 2022b).

Following D1, dextral transpression (D2) occurred during the middle to late Carboniferous (ca. 330–310 Ma), forming subvertical fabrics S2 associated with dextral shear (Jacob et al. 2021a; Simonetti et al. 2018 2020; Vanardois et al. 2022c, 2022b; Von Raumer and Bussy 2004), and conjugate sinistral shear localized in the Pelvoux Massif (Fréville et al. 2022; Strzerzynski et al. 2005). Phase D2 was coeval with horizontal flow of the partially molten crust that started during crustal thickening and then persisted until the early stages of exhumation of the deep-seated rocks (Fréville et al. 2022; Jacob et al. 2022; Vanardois et al. 2022b, c). The phase D2 in the ECM is correlated with a plate-scale dextral transcurrent regime caused by the anti-clockwise rotation of Gondwana relative to Laurussia, which affected a large part of the Variscan Belt (Ballèvre et al. 2018; Chardon et al. 2020; Edel et al. 2018).

Around 305 Ma, transpression evolved into transtension (D3), leading to crustal thinning and locally forming S3 flat-lying foliations (Fernandez et al. 2002; Fréville et al. 2022; Guillot et al. 2009; Vanardois et al. 2022c) (Fig. 3b, c). Concurrently, a second low-pressure anatectic event occurred, forming Crd-bearing migmatites (Barféty and Pêcher 1984; Fréville et al. 2022).

The Variscan tectono-metamorphic evolution was also characterized by intense magmatic activity, recorded from the convergence onset (late Devonian–early Carboniferous) to the late-collisional stages (late Carboniferous–early Permian). Geochemical and petrological investigation of these magmatic series occurred predominantly during the 1980s to the late 1990s (Banzet 1987; Debon et al. 1998; Debon and Lemmet 1999; Ménot 1987; Vivier et al. 1987). However, the classification scheme outlined in these studies appears somewhat outdated and requires revisions to align with the latest research on magmatism in other regions of the European Variscides. Thus, a detailed description of these series with an updated classification, incorporating our latest geochronological, petrological, and geochemical data, is presented further down in the Result section.

Analytical methods

U–Pb dating

Twenty-two samples of the different Variscan magmatic series and older igneous protoliths (orthogneiss) (Fig. 2) have been dated using U–Pb geochronology on zircon performed by in situ Laser Ablation Inductively Coupled Plasma Mass Spectrometry (LA-ICP-MS) at the GeOHeLiS

Table 1 Summary of geographic location, rock types, and U–Pb geochronological results for analyzed samples

Sample	Group	Pluton/locality	Mineral assemblage	MME	Lat° (WGS84)	Long° (WGS84)	U–Pb age (±2σ)	MSWD	N	Interpretation	Geo-chemical analysis
MCE33	MgG	Sept-Laux granite inner facies	Qtz + Pl + Kfs + Bt ± Ttn	yes	N45°12′46.03"	E06°04′7.84″	326 ± 3 Ma (CA)	1.4	7	Magmatic age	Yes
							464 ± 8 Ma (CA)	2	4	Inherited age	
							566 ± 7 Ma (LI)	2.5	4	Inherited age	
MCE39	MgG	Sept-Laux granite outer facies	Qtz + Pl + Kfs + Bt	yes	N45°12′38.79"	E06°3′47.94"	348 ± 3 Ma (CA)	0.71	12	Magmatic age	Yes
MCE42	MgG	Coarse-grained RNLF granite	Qtz + Pl + Kfs + Bt ± Ms	yes	N45°6′48.21"	E06°4′45.92"	308 ± 3 Ma (LI)	0.59	6	Magmatic age	Yes
MCE150	MgG	Fine-grained RNLF granite	Qtz + Pl + Kfs + Bt ± Ms	yes	N45°9′48.93"	E06°6′9.33"	310 ± 5 Ma (LI)	0.35	11	Magmatic age	Yes
							332 ± 3 Ma (CA)	1.6	5	Inherited age	
MCE151	MgG	Alpetta granite	Qtz + Pl + Kfs + Bt	yes	N45°9′52.07"	E06°6′8.02"	339 ± 2 Ma (CA)	1.2	12	Magmatic age	No
MCE152	MgG	Deformed RCLF granite	Qtz + Pl + Kfs + Bt ± Ms	yes	N45°9′56.44"	E06°6′9.08"	305 ± 3 Ma (LI)	0.31	6	Magmatic age	Yes
MCE181	MgG	Fine-grained Rochail granite	Qtz + Pl + Kfs + Bt	yes	N45°1′49.91"	E06°2′47.64"	337 ± 3 Ma (CA)	1.5	8	Magmatic age	Yes
MCE182	MgG	Coarse-grained Rochail granite	Qtz + Pl + Kfs + Bt ± Ttn	yes	N45°1′32.04"	E06°2′55.87"	346 ± 5 Ma (CA)	1.8	13	Magmatic age	Yes
MCE301	MgG	Bans granite	Qtz + Pl + Kfs + Bt + Amph	no	N44°50′17.35"	E06°21′8.35"	305 ± 2 Ma (CA)	1.4	21	Magmatic age	Yes
MCE315	MgG	Riéou Blanc granite	Qtz + Pl + KFs + Bt	no	N44°50′9.54"	E06°22′35.56"	301 ± 2 Ma (CA)	1.3	23	Magmatic age	Yes
MCE342	MgG	Entraigues granite	Qtz + Pl + Kfs + Bt + Ms	no	N44°53′22.54"	E05°55′54.59"	339 ± 6 Ma (CA)	0.76	4	Magmatic age	Yes
							365 ± 5 Ma (CA)	0.78	5	Inherited age	
							465 ± 7 Ma (CA)	1.8	4	Inherited age	
							508 ± 7 Ma (CA)	0.41	5	Inherited age	
							639 ± 11 Ma (CA)	0.63	3	Inherited age	
MCE142	FeMgG	Etages granite	Qtz + Pl + Kfs + Bt ± Ms ± Grt	no	N44°56′0.79"	E06°12′37.50"	299 ± 3 Ma (CA)	1.5	8	Magmatic age	Yes
MCE167c	FeMgG	Weakly foliated BP granite	Qtz + Pl + Kfs + Bt ± Ms	no	N44°56′18.68"	E06°17′42.03"	303 ± 2 Ma (CA)	0.74	12	Magmatic age	Yes
							329 ± 4 Ma (CA)	1.12	3	Inherited age	
MCE168	FeMgG	Coarse-grained BP granite	Qtz + Pl + Kfs + Bt ± Ms	no	N44°56′15.86"	E06°17′40.42"	278 ± 6 Ma (LI)	0.48	7	Posterior thermal event	Yes
							301 ± 3 Ma (LI)	0.29	5	Magmatic age	
MCE183b	FeMgG	Cray granite	Qtz + Pl + Kfs + Bt + Ms + Crd	no	N44°56′46.95"	E06°14′39.44"	274 ± 3 Ma (CA)	1.2	6	Posterior thermal event	Yes
MCE323v	FeMgG	Bourg granite	Qtz + Pl + Kfs + Bt + Amph	yes	N44°49′37.04"	E06°14′28.95"	317 ± 4 Ma (CA)	1.1	5	Magmatic age	No
							448 ± 7 Ma (CA)	1.6	4	Inherited age	

Table 1 (continued)

Sample	Group	Pluton/locality	Mineral assemblage	MME	Lat° (WGS84)	Long° (WGS84)	U–Pb age (± 2σ)	MSWD	N	Interpretation	Geochemical analysis
JB-20–07	FeMgG	Bourg granite	Qtz + Pl + Kfs + Bt + Amph	yes	N44° 49′ 32.57"	E06° 13′ 37.6"	318 ± 3 Ma (CA)	1.5	18	Magmatic age	Yes
JB-20–11	UHKG	Colle-Blanche qtz-monzonite	Pl + Qtz + Kfs + Amph + Bt + Chl + Ap + Ttn	yes	N44° 45′ 45.81"	E06° 10′ 1.89"	307 ± 3 Ma (CA)	1.4	13	Magmatic age	Yes
JB-19–30	UHKG	Olan qtz-syenite	Kfs + Bt + Cpx ± Qtz ± Pl ± Amph	yes	N44° 50′ 19.02"	E06° 14′ 13.92"	328 ± 2 Ma (CA)	0.48	29	Magmatic age	Yes
JB-19–58	UHKG	Olan qtz-syenite	Amph + Kfs ± Qtz ± Bt ± Pl	yes	N44° 50′ 39.25"	E06° 14′ 57.09"	324 ± 2 Ma (CA)	0.42	28	Magmatic age	Yes
MCE281a	OG	Glacier Blanc orthogneiss	Qtz + Pl + Kfs + Bt + Amph + Ttn	no	N44°55′56.40"	E06°24′38.96"	279 ± 3 Ma (CA)	0.62	7	Posterior thermal event	No
							331 ± 4 Ma (CA)	0.48	10	Magmatic age	
MCE324v	OG	Crupillouse orthogneiss	Qtz + Pl + Kfs + Ms + Bt	no	N44°49′16.19"	E06°11′42.33"	468 ± 4 Ma (LI)	1.8	7	Magmatic age	No
							592 ± 15 Ma (LI)	3.8	6	Inherited age	

MME, microgranular mafic enclaves; RNLF, Roche-Noire—La Fare; BP, Bérarde—Promontoire

analytical Platform (Rennes), Géosciences Montpellier and BRGM (Orléans). Locations of samples are given in Table 1 and detailed descriptions for each sample are available in the supplementary materials. Zircon grains have been separated using classical dense liquor separation at the Department of Mineralogy and Mineral Raw Materials of the Bulgarian Academy of Sciences (Sofia, Bulgaria) and at BRGM (Orléans, France). Zircon grains have been carefully handpicked under a binocular microscope to represent all variations of size, shape and color, placed in epoxy mounts and polished to expose the center of the grains. Zircon grains were imaged by cathodoluminescence (CL) at Besançon in the Femto-st laboratory, Franche-Comté University, using a FEI Quanta 450 W scanning electron microscope (SEM), at BRGM using a TESCAN Mira 3 XMU SEM and at ISTerre Grenoble using a TESCAN Vega 3 SEM.

In-situ U–Pb isotopic analyses have been performed by LA-ICPMS, with spot sizes of 25–26 µm, using an ESI NWR193 UC excimer laser coupled to a 7700 × Agilent quadrupole ICP-MS at GeOHeLiS (Rennes), a Compex 102 Lambda-Physik excimer laser coupled to a Plasmaquad II quadrupole ICP-MS at Géosciences Montpellier and a Cetac Excite 193 nm excimer laser coupled to X series II quadrupole ICP-MS at BRGM.

Details of the analytical protocol are available in the online supplementary materials and were described by Manzotti et al. (2016) for Rennes and Bosch et al. (2016) for Montpellier. Isotopic data were corrected by using zircon standard 91,500 (Wiedenbeck et al. 1995; Montpellier Géosciences and BRGM analyses) and zircon GJ-1 (Jackson et al. 2004; GeOHeLiS Rennes analyses). For analyses at Géosciences Montpellier, the quality check was done with the GJ-1 standard (608.5 ± 1.5 Ma, Jackson et al. 2004), which returned an age at 604.5 ± 2.0 Ma ($MSWD_{(C+E)}$ = 0.41, n = 14). For the other analyses, the Plešovice standard was used (338 ± 1 Ma, Sláma et al. 2008), which gave ages of 340.2 ± 1.4 Ma (MSWD(C + E) = 0.63, n = 58, BRGM), 337.4 ± 1.1 Ma (MSWD(C + E) = 1.2, n = 46, GeOHeLis Rennes session 1) and 335.4 ± 1.9 Ma (MSWD(C + E) = 1.4, n = 15, GeOHeLis Rennes session 2). All these ages overlap with the Plešovice standard age at 338 ± 1 Ma (Sláma et al. 2008) and all together, the data yield a concordia age at 338.0 ± 0.83 Ma (MSWD(C + E) = 1, n = 119) (Fig. S1). It is possible that the data acquired at BRGM yield slightly older dates than data from the second session at Rennes, but it will not affect the main results of our study. Data reduction has been performed with the GLITTER® software package developed by Macquarie Research Ltd. (Griffin 2008) and by the Iolite data-reduction scheme (Paton et al. 2011) for the second session at GeOHeLis Rennes. Concordia ages and diagrams have been generated either with Isoplot/Ex (Ludwig 2003) or the IsoplotR package (Vermeesch 2018). Individual uncertainties are quoted at 2σ level and the

confidence level for weighted averages is 95%. Uncertainty propagation is by quadratic addition according to Horstwood et al. (2016), including age uncertainty of reference material. All data are reported in Table S1 in the electronic supplement.

Major, trace-element and isotope geochemistry

Whole-rock geochemical analyses were performed at the Service d'Analyse des Roches et Minéraux (SARM) in Nancy, using a Thermo Fischer iCap6500 ICP-OES for major oxides and an iCapQ ICP-MS for minor and trace elements. Details about the analytical procedures for whole-rock geochemical analyses are described in Carignan et al. (2001).

Fifteen samples were analyzed for Sr and Nd radiogenic isotopes at SEDISOR in Brest (MCE33, MCE39, MCE42, MCE150, MCE152, MCE181, MCE182, MCE301, MCE315, MCE342, MCE142, MCE167c, MCE168 and MCE183a). About 200 mg of samples were weighted and dissolved in Savillex beakers in a mixture of ultrapure Quartex HF (24N, 2 ml), HNO_3 (14N, 1 ml) and $HClO_4$ (12N, 0.1 ml) for 4 days at 160 °C on a hot plate. Sr and Nd fractions were chemically separated using the Triskem TRU. Spec, Sr.Spec and Ln.Spec-specific resins following column chemistry procedure modified from Pin and Zalduegui (1997). Strontium and Nd isotope compositions were measured by 9 collectors in static mode on a Thermo TRITON TIMS (Thermal Ionization Mass Spectrometer) at the PSO (Pôle de Spectrométrie Océan) in Brest, France. All measured Sr and Nd ratios were normalized to $^{86}Sr/^{88}Sr = 0.1194$ and $^{146}Nd/^{144}Nd = 0.7219$, respectively. During the course of analysis, Sr isotope compositions of the NBS987 standard solution yielded $^{87}Sr/^{86}Sr = 0.710267 \pm 4$ ($n = 4$, recommended value 0.710250); Nd standard solution JNdi (Tanaka et al. 2000) analyses gave a $^{143}Nd/^{144}Nd$ value of 0.512108 ± 6 ($n = 2$, recommended value 0.512100).

Isotopic measurements were also carried out at the SARM in Nancy for samples JB-19–30, JB-19–58, JB-20–07 and JB-20–11. 100–200 mg of powdered samples were dissolved into a mixture of concentrated HNO_3 and HF heated to 115 °C for 24 to 48 h, followed by concentrated HCl at 125 °C for 24 h. Sr and Nd were isolated via ion-exchange chromatography using Sr.Spec, Tru.Spec and Ln.spec resins, following the procedure described in Pin et al. (1994) and Pin and Zalduegui (1997). Sr and Nd isotopes were analyzed using respectively a Triton Plus TIMS and a Neptune Plus MC ICP-MS both operated in static multi-collection mode. The $^{87}Sr/^{86}Sr$ ratios were corrected for mass bias assuming $^{87}Sr/^{88}Sr = 0.1194$, and $^{143}Nd/^{144}Nd$ ratios were corrected to $^{146}Nd/^{144}Nd = 0.7219$ (Luais et al. 1997). Internal standards NBS 987 and JNdi-1 were used respectively for Sr and Nd. $^{87}Rb/^{86}Sr$ and $^{147}Sm/^{144}Nd$ were calculated using Rb, Sr, Sm and Nd content determined from whole rock analysis.

The decay constants applied for age-correction of isotopic ratios are from Steiger and Jäger (1977) for Sr and Lugmair and Marti (1978) for Nd. The εNd_i values were obtained using the chondritic uniform reservoir (CHUR) composition of Bouvier et al. (2008).

Variscan magmatism in the ECM

We compiled ca. 482 whole-rock analyses of Carboniferous granitoids and associated mafic/intermediate rocks, incorporating our newly acquired analyses and existing data from published studies, as well as Ph.D. and Master degree works conducted between 1970 and 1992. The dataset underwent rigorous filtering to remove spurious analyses, including those with a bad total of oxides (Total > 102 wt% or < 97 wt%) or abnormally high aluminosity. The complete dataset, including the references, is accessible in Table S2 in the electronic supplements, together with the R script used for processing and plotting geochemical diagrams.

Variscan magmatic activity in the ECM spans from the pre-collisional stages (late Devonian–early Carboniferous, ca. 370–350 Ma) to the post-collisional stages (late Carboniferous–early Permian, ca. 310–295 Ma). Three discernible series, characterized by emplacement age and composition, include: (i) a pre-collisional, tholeiitic to low-K calc-alkaline series (Carme and Pin 1987; Ménot 1987); (ii) syn/post-collisional high-K calc-alkaline, peraluminous granitoids (Banzet 1987; Debon et al. 1998; Debon and Lemmet 1999); (iii) a syn/post-collisional (ultra)-high-K, Mg-rich metaluminous series (Debon et al. 1998) akin to the durbachites and vaugnerites found in neighboring Variscan massifs (Couzinié et al. 2016; Rossi and Cocherie 1991; Tabaud et al. 2015; Von Raumer et al. 2014). While the first series is not the primary focus of the present study, it is briefly described here for completeness.

Pre-collisional, tholeiitic to low-K calc-alkaline bimodal series

Plutonic and volcano-sedimentary rocks of this group are exposed in the southern part of Belledonne and western part of Pelvoux Massifs (VSU, Figs. 1, 2) (Ménot 1987), and underwent greenschist to amphibolite-facies metamorphism during the Visean. The igneous part mainly consists of highly-deformed, alternating layers of leucocratic plagioclase-rich gneisses and amphibolites, cross-cut by less-deformed sills and stocks of meta-trondhjemites, meta-basalts and meta-diorites (Ménot 1987). These rocks exhibit low-K, sodic, metaluminous compositions, displaying affinities either to enriched tholeiites or to low-K calc-alkaline series (Carme and Pin 1987; Ménot 1987; Ménot

and Paquette 1993). In the ECM, the emplacement age is constrained between ca. 370 and 350 Ma by U–Pb dating of trondhjemitic sills and K–Ar dating on amphibole (Fréville et al. 2018; Guillot and Ménot 2009; Ménot et al. 1987). A similar pre-collisional magmatism was also described in the southern part of the Aiguilles-Rouges Massif (Dobmeier et al. 1999). Its tectonic significance remains debated (part of this series might actually be of Cambrian–Ordovician age), but the most common interpretation invokes a late Devonian back-arc environment (Guillot and Ménot 2009; Vanardois et al. 2022a), similar to the Brévenne Unit in the northeastern Massif Central (Faure et al. 2009; Pin and Paquette 1997)), the Klippen Belt in the Southern Vosges Massif (Skrzypek et al. 2012) or the Moldanubian zone in the Bohemian Massif (Janoušek et al. 2014; Schulmann et al. 2009).

Syn- to post-collisional, high-K calc-alkaline granitoids

This suite consists of large granitoid intrusions (up to ca. 100 km^2 for the Sept-Laux Pluton) and smaller satellite intrusions emplaced at the middle and lower crustal levels during the middle to late-Carboniferous. Most of these plutons show magmatic and/or high-T subsolidus fabrics oriented parallel to the regional vertical S2 foliation (Fig. 3), suggesting a syn-kinematic D2 emplacement (Fréville et al. 2022; Strzerzynski et al. 2005; Vanardois et al. 2022c). These granitoids contain variable amounts of mafic enclaves, which form either decameter to hectometer-size bodies, especially in the Rochail granite (De Boisset 1986), or swarms of decimeter to meter-size enclaves elongated parallel to the granite foliation (Fig. 4a).

Geochronological data for the granitoids of Belledonne, Grandes Rousses and Pelvoux Massifs are relatively scarce. Several intrusions were dated by single-zircon evaporation (Cannic et al. 1998; Debon et al. 1998; Guerrot and Debon 2000) at 343 + 11/-10 Ma (Rochail), 302 ± 5 Ma (Turbat-Lauranoure), 335 ± 13 Ma (Sept-Laux), 343 ± 16 Ma (St Colomban) and 341 ± 13 Ma (Lauzière monzogranite). This lack of precise and accurate geochronogical data contrast with the northern part of ECM (Aar Massif, Mont-Blanc), where the timing of Variscan and pre-Variscan magmatism is better constrained (Bussien-Grosjean et al. 2018; Bussy et al. 2000; Ruiz et al. 2022; Vanardois et al. 2022c). In particular, in the Aar Massif, a recent study by Ruiz et al. (2022) has identified four Variscan magmatic events at ca. 348, 333, 309 and 298 Ma.

Compositions range from Bt–Amp granodiorite to ordinary peraluminous Bt–Ms granite (Fig. 5a, Debon and Le Fort 1983), with SiO_2 between 65.8 and 77.0 wt% (excluding the top and bottom 5% to account for possible outliers). There is no discernable B–A (maficity–aluminosity) correlation (Fig. 5b). The granitoids are highly potassic (K_2O = 3.3–5.7 wt% and mass ratio K_2O/Na_2O = 0.71–1.91, Fig. 5c, d) and alkali-calcic to calc-alkalic (Fig. 5e; Frost et al. 2001), categorizing them as Potassic Calc-alkaline Granitoids (KCG) in the classification of Barbarin (1999). These granitoids, common in the internal domains of the Variscan Belt (eastern Massif Central, Vosges, Black Forest and Bohemian Massif; (Jacob et al. 2021b; Janoušek et al. 2010; Moyen et al. 2017; Tabaud et al. 2015), reflect hybridization between crustal and mantle-derived magmas (Couzinié et al. 2016; Jacob et al. 2021b; Moyen et al. 2017). Debon and Lemmet (1999) subdivided these granitoids into two sub-series based on Mg# (molar ratio Mg/(Fe + Mg)) (Fig. 5f).

The high-Mg# series (MgG) comprises mainly Amph + Bt ± Ms granodiorites and Bt ± Ms ± Amph granites, rich in mafic enclaves (Fig. 4b) and likely emplaced during the Visean (ca. 340–330 Ma). Some plutons exhibit cross-cutting relationships between an older, deformed facies rich in mafic enclaves, and a younger, leucocratic and less deformed facies (Fig. 4c, d). The MgG suite mainly intruded the (non-anatectic) Variscan mid–upper crust, except a few plutons in the Inner Pelvoux Massif (Fig. 2).

The low-Mg# series (FeMgG) consists of Bt + Ms ± Amph granites, with fewer mafic enclaves (Fig. 4e), presumably emplaced during the late Carboniferous to earliest Permian (ca. 305–295 Ma). The FeMgG plutons mostly intruded the migmatitic basement of the Inner Pelvoux (Fig. 2) and are also found further north in the Mont-Blanc and Aiguilles Rouges Massifs (Fig. 1). These were all emplaced between 310 and 300 Ma (Bussy et al. 2000; Vanardois et al. 2022c).

Both sub-series share a similar composition, with intra-group variation larger than the inter-group difference for most elements (Figs. 5, 6). However, differences in Mg# are observed (Fig. 5f), with median Mg# of 0.48 and 0.37 for the MgG and FeMgG, respectively. The FeMgG also appear slightly more potassic and siliceous (median mass ratio K_2O/Na_2O = 1.38, median SiO_2 = 73.7 wt%) than the MgG (median K_2O/Na_2O = 1.06, median SiO_2 = 71.7 wt%). Minor and trace element concentrations also differ, with MgG generally richer in LILE (Ba, Sr, Pb) and some HFSE (Th, U, Zr, Hf), while FeMgG contains more HREE. Despite these distinctions, trace-element patterns exhibit substantial overlap, showcasing enrichment in LILE and LREE relative to HREE, negative Nb–Ta and Ti anomalies and pronounced positive anomalies in Pb compared to primitive mantle (Fig. 6a).

The Sr–Nd isotopic compositions are similar between the FeMgG and MgG. For most samples, initial $^{87}Sr/^{86}Sr_i$ recalculated to their emplacement ages range between 0.7046 and 0.7070 and εNd_i between −5.8 and −1.2 (Table 2, Fig. 7). Exceptions include the Cray granite (FeMgG), with a highly radiogenic Sr signature ($^{87}Sr/^{86}Sr_i$ = 0.7126) and a εNd_i = −3.2, and the Bérarde–Promontoire and Roche

Fig. 4 Field photos of the different magmatic facies. **a** Swarm of elongated durbachitic (mafic ultrapotassic. UHKM) enclaves in a boulder of the Sept-Laux granite (MgG). **b** Close-up view of one enclave, showing digitated borders with a reaction rim enriched in mafic minerals (Bt, Amp). Clusters of dark minerals in the granite could represent xenocrysts from the mafic enclaves entrained into the melt. **c**, **d** Contact between older and younger intrusions in the Sept-Laux granite and at the contact between Alpetta (older) and Roche-Noire (younger) plutons. Older facies are characterized by a high proportion of mafic to intermediate enclaves (durbachites) and penetrative ductile deformation, while the younger facies are more leucocratic and undeformed. **e** Close-up view on a boulder of Bérarde-Promontoire granite (FeMgG), showing mingling between two different facies. **f** Sample of the Olan quartz syenite, with large K-feldspar crystals surrounded by Bt + Amph

Noire granites (respectively FeMgG and MgG), with subchondritic signatures: $^{87}Sr/^{86}Sr_i$ (0.7008–0.7013) and εNd_i between −3.2 and −1.1.

Syn- to post-collisional, (ultra)-high Mg–K metaluminous series (durbachites)

Subordinate amounts of mafic to intermediate, Mg–K rich rocks (durbachites) are found in the ECM basement, forming hectometer to kilometer-sized plutonic bodies composed of K-rich monzodiorite, quartz monzonite and quartz syenite (Debon et al. 1998). Examples include the Olan quartz syenite in central Pelvoux (Figs. 2, 4f), or enclaves in high-K calc-alkaline granitoids (De Boisset 1986; Debon et al. 1998), especially in the Sept-Laux, Grun and Rochail Plutons (Figs. 2, 4a–d). They also occur as mafic dykes intruding the basement (Laurent 1992), or as scattered 0.1–1 m-wide lenses within highly deformed migmatitic domains. Mineral assemblages are dominated by Kfs + Amph + Bt ± Cpx (either as relics, or stable with Bt + feldspars) (Fig. 4f), with subordinate Pl and Qtz, and Ap + Ttn + Zrc as common accessory minerals. These rocks exhibit significant heterogeneity. They range from (quartz)-syenite to quartz-monzodiorite (Fig. 5a), with SiO_2 ranging from 48 to 64 wt% and K_2O from 3.3 to 7.3 wt% (Fig. 5c). They are alkalic to alkali-calcic (Fig. 5e), metaluminous to slightly peraluminous and display a clear negative B–A correlation (Fig. 5b). They are characterized by high Mg# (0.5–0.72), elevated Cr–Ni contents (Cr = 17–600 ppm, Ni = 10–442 ppm) and high K_2O/Na_2O ratios (0.89–4.35). Thus, most of them are highly potassic ($K_2O/Na_2O > 1$) to ultrapotassic ($K_2O/Na_2O > 2$). These rocks are notably enriched in incompatible elements, in particular LILE (Rb, Ba, Sr), Th, U and LREE, with concentrations exceeding 50 to 100 × that of the primitive mantle, and reaching up to 500 × enrichment for Th and U in extreme samples (Fig. 6). They are also richer in all REE (except last HREE), LILE and HFSE than the HK calc-alkaline granitoids, despite being less differentiated (lower SiO2 content). However, trace-element patterns show a similar shape as the HK calc-alkaline granitoids, with LREE enrichment relative to HREE, negative Nb and Ti anomalies and strongly positive Pb anomalies (Fig. 6a).

The Sr–Nd isotope data have been acquired for two plutonic formations, the Colle-Blanche quartz monzonite (1 sample) and the Olan quartz syenite (4 samples), in an enclave from the Rochail granite (JB-20–01), and in a biotite-rich mafic enclave (presumably a dismembered lamprophyre dyke) sampled in the migmatitic basement of the inner Pelvoux (JB-19–36), close to the Olan intrusion (Table S3, Fig. 7). The latter is a clear outlier with very radiogenic Sr ($^{87}Sr/^{86}Sr_i = 0.7163$) and low εNd_i (−6.1). The other samples also present high $^{87}Sr/^{86}Sr_i$ (0.7064–0.7094) and low εNd_i (−5.5 to −3.9), which plot respectively in the upper and lower ranges of values measured in the high-K calc-alkaline granitoids (FeMgG and MgG, Fig. 7).

Zircon U–Pb geochronology

New U–Pb data have been acquired on zircon grains from twenty-two samples of granite and durbachite. A few orthogneisses (OG) sampled in the Pelvoux Massif, which presumably corresponds to lower Paleozoic basement lithologies, have also been dated. Detailed presentation of CL imaging of zircon textures, U–Th–Pb analyses, U–Pb results and diagrams, and statistics for each sample are in the online supplementary materials. We summarize here the most important features of each magmatic group (i.e. MgG, FeMgG, UHKM and OG), with representative concordia diagrams of a few samples from each group. All the concordia diagrams are available in the online supplements (Appendix 1), together with the complete dataset (Table S1).

Zircon textures and shapes

Zircon grains present a variety of textures and shapes, which can greatly vary from sample to sample, but a broad generalization can be made within each group.

MgG samples show heterogeneous zircon populations, having a range of sizes (from 50 to 350 µm) and shapes (aspect ratios between 1 and 4) (Fig. 8a–k). Most of them show idiomorphic morphologies with concentric oscillatory zoning, but some grains show irregular or broken shapes. A few grains display more complex internal zoning with core–rim relationships. Typically, these grains show a CL-bright core with an irregular or slightly rounded shape, surrounded by a CL-darker rim commonly displaying oscillatory zoning. Very scarce grains are CL-dark without concentric zoning or thin CL-dark rim.

Zircon grains in FeMgG samples typically occur as elongated, prismatic grains (aspect ratios between 2 and 4) ranging from 50 to 400 µm in length (Fig. 8l–q). As for the MgG samples, most zircon populations from FeMgG samples show idiomorphic grains with concentric oscillatory zoning. Several grains display core–rim relationships, both cores and rims showing oscillatory zoning. Two samples show different zircon features: (i) zircon grains from sample MCE142 are elongated, CL-dark and display irregular or patchy zoning, without oscillatory zoning; (ii) sample MCE183b displays idiomorphic elongated zircon grains with or without concentric zoning, and other grains displaying resorbed cores surrounded by thin rims without concentric zoning.

The UHKM samples come from two different intrusive formations: the Olan quartz syenite and the Colle-Blanche Plutonic

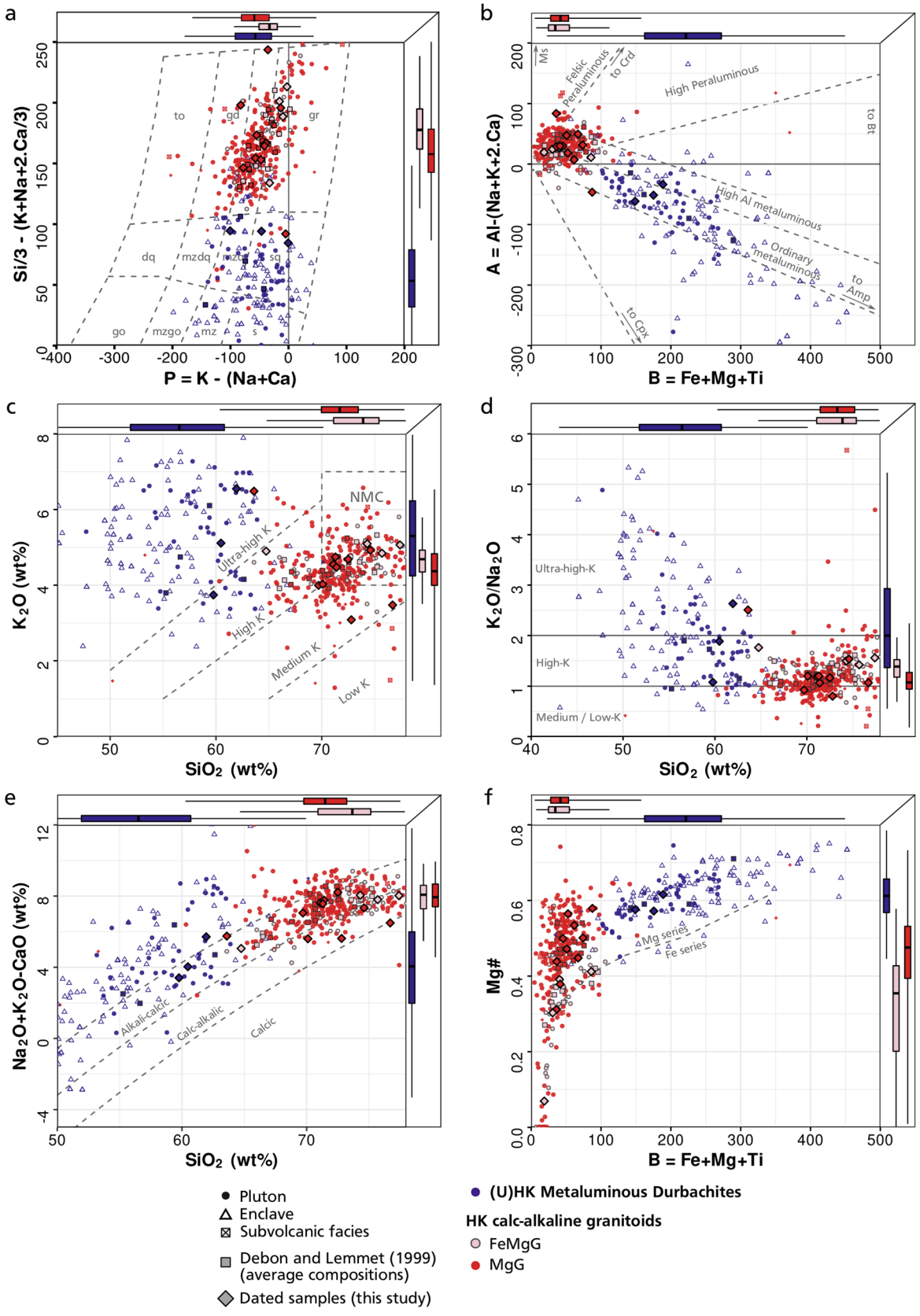
a
Si/3 - (K+Na+2.Ca/3)
P = K - (Na+Ca)
to
gd
gr
dq
mzdq
mzgd
sq
go
mzgo
mz
s
b
A = Al-(Na+K+2.Ca)
B = Fe+Mg+Ti
Ms
Felsic Peraluminous
to Crd
High Peraluminous
to Bt
High Al metaluminous
Ordinary metaluminous
to Amp
to Cpx
c
K2O (wt%)
SiO2 (wt%)
NMC
Ultra-high K
High K
Medium K
Low K
d
K2O/Na2O
SiO2 (wt%)
Ultra-high-K
High-K
Medium / Low-K
e
Na2O+K2O-CaO (wt%)
SiO2 (wt%)
Alkali-calcic
Calc-alkalic
Calcic
f
Mg#
B = Fe+Mg+Ti
Mg series
Fe series
Pluton
Enclave
Subvolcanic facies
Debon and Lemmet (1999) (average compositions)
Dated samples (this study)
(U)HK Metaluminous Durbachites
HK calc-alkaline granitoids
FeMgG
MgG

◂**Fig. 5** Major-element geochemistry of Variscan igneous rocks from the Belledonne, Pelvoux and Grandes Rousses massifs. **a** P-Q classification diagram of Debon and Le Fort (1983). from top left to bottom right: to—tonalite; gd—granodiorite; gr—granite; dq—quartz-diorite; mzdq—quartz-monzodiorite; mzq—quartz monzonite; sq—quartz syenite; go—gabbro; mzgo—monzogabbro; mz—monzonite; s—syenite. **b** Aluminosity versus maficity (A–B) diagram (Debon and Le Fort 1983). Grey fields are from Jacob et al. (2021b). **c** K_2O versus SiO_2 diagram (Peccerillo and Taylor 1976). Separation between low/medium/high/ultra-high-K domains after Jacob et al. (2021b). NMC: near-minimum melt compositions close to the granite eutectic. **d** K_2O/Na_2O versus SiO_2 diagram highlighting the distinction between low-/medium-K, high-K and ultra-high-K series according to Foley et al. (1987). **e** Modified alkali–lime index (MALI: Na_2O+K_2O-CaO) versus SiO_2 (Frost et al. 2001). **f** Mg# versus B diagram (Debon and Le Fort 1988). Boxplots on the side of each panel show the distribution within each group (MgG, FeMgG, UHKM). Data from: this study; Aumaitre et al. 1985; Costarella 1987; De Boisset 1986; Debon et al. 1998; Debon and Le Fort 1988; Gasquet 1979; Giorgi 1979; Le Fort 1971; Negga 1984; Oliver 1994; Poncerry 1981; Simeon 1979; Verjat 1981. Averaged data from Debon and Lemmet (1999): squares; samples dated in this study: diamonds

Complex, which display very different zircon morphologies. Zircon grains from the Olan quartz syenite are remarkably homogeneous. They are usually 100–300 µm long, euhedral prisms with aspect ratios between 1.3 and 2.5, and contain numerous inclusions of apatite (Fig. 8r, s). The CL imaging reveals common concentric oscillatory and/or sector zoning with an absence of core-rim relationships. In contrast, the Colle-Blanche quartz monzonite (JB-20–11) contains a very heterogeneous population of zircon. They yield 80–200 µm long grains, euhedral to subhedral, prismatic to slightly rounded, with aspect ratios between 1.5 and 3 that commonly display complex, patchy zoning and/or core–rim relationships (Fig. 8t).

For Orthogneisses, zircon grains from sample MCE281a (Pelvoux Massif) are heterogeneous, having sizes ranging between 100 and 250 µm and aspect ratios between 1 and 3 (Fig. 8u). Zircon crystals are idiomorphic and show concentric, oscillatory zoning and few of them have CL-bright cores. Zircon grains from sample MCE324v (Crupillouse

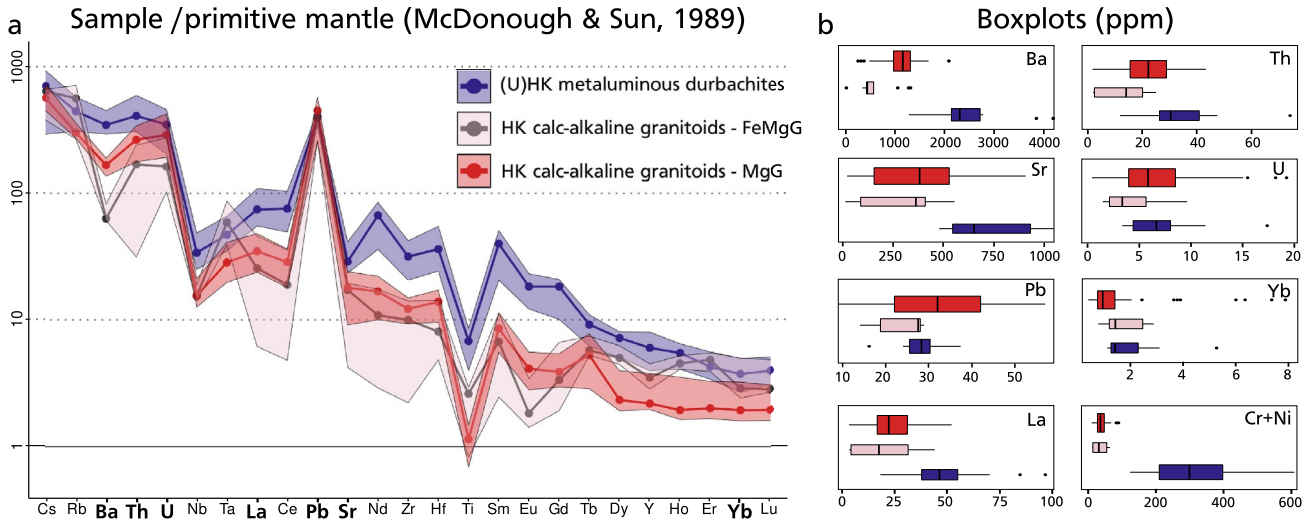

Fig. 6 Trace-element geochemistry. **a** Trace-element patterns normalized to the primitive mantle composition (Sun and McDonough 1989), separated by geochemical groups (MgG, FeMgG, UHKM). Central patterns (solid lines) correspond to the median composition for each group, and the shaded envelopes to the interquartile [q25; q75] range. **b** Boxplots for a selected subset of trace and minor elements in ppm

Table 2 Zircon saturation temperatures calculated for three samples of the metaluminous ultra-potassic plutons (durbachites), using the calibration of Boehnke et al. (2013)

Pluton	Sample	B	M	Zr (ppm)	Zr sat T (°C)	inh. zrc/xenocrysts
Olan qtz-syenite	JB-19–30	175.32	1.84	346.5	838	No
Olan qtz-syenite	JB-19–58	148.93	1.88	343.4	837	No
Colle Blanche qtz-monzonite	JB-20–11	188.76	1.7	207.2	778	Yes

B = Fe + Mg + Ti (millications)

M = (Na + K + 2.Ca)/(Al.Si) (in cation percent)

inh. zrc: inherited zircon

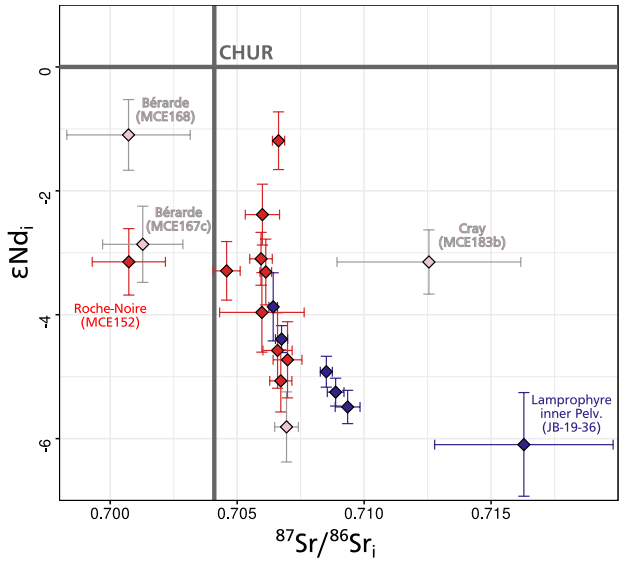

Fig. 7 Sr–Nd isotopic compositions recalculated to the respective emplacement ages (εNdi vs. $^{87}Sr/^{86}Sr_i$). CHUR: Chondritic Uniform Reservoir model composition from Bouvier et al. (2008)

orthogneiss) are fractured or partially resorbed, with sizes ranging between 50 and 300 µm and aspect ratios between 1 and 4 (Fig. 8v). A concentric zoning is sometimes visible.

Independently of the rock groups (MgG, FeMgG, UHKM, OG), most zircon grains (> 90%) show high Th/U (> 0.1) and high U concentrations (> 200 ppm). This is especially true in the youngest Carboniferous–early Permian populations (Fig. 9a). However, a few zircon analyses yielded very low Th/U (down to ca. 0.002), especially in quartz monzonite JB-20–11.

U–Pb dating results

The complete geochronological dataset, plotted in Fig. 9b, consists of 626 zircon spot analyses, out of which 535 are less than 10% discordant [i.e. having $100 \times (1 - \text{age}_{206Pb/238U}/\text{age}_{207Pb/235U}) < 10$]. Most of these concordant or slightly discordant analyses yield late Devonian to early Permian U–Pb dates (360–280 Ma), with two main peaks in the distribution centered at ca. 330 Ma and 305 Ma respectively (Fig. 9c). Older zircon grains are observed, which yield mainly early Paleozoic (ca. 500–430 Ma) and Neoproterozoic (ca. 600–550 Ma) U–Pb dates. Finally, several spots yielded much older, Paleoproterozoic to Mesoarchean U–Pb dates up to ca. 3 Ga (Fig. 9b) with a noticeable lack of Mesoproterozoic dates.

However, this distribution varies between the different rock groups. In the MgG, two Carboniferous peaks are centered at ca. 330 Ma and 305 Ma, while older peaks are visible around 550 and 450 Ma (Fig. 9b). The zircon spectra for the FeMgG feature a well-marked peak centered at ca. 300 Ma, a less pronounced peak at ca. 320 Ma and a younger Permian peak at ca. 275 Ma, plus some older dates mostly centered around 450 Ma. The UHKM rocks yield a sharp peak centered at ca. 325 Ma, with older grains scattered from ca. 450 Ma to 350 Ma. Finally, the OG contains only two samples, with too little data (35 analyses which are less than 10% discordant) to obtain reliable statistics on the age distribution.

In the *MgG group*, zircon U–Pb dates follow a complex distribution, with multiple populations of concordant and discordant data. A main cluster of concordant Carboniferous U–Pb dates is generally observed (Fig. 10a–c), which mainly consists of zircon grains with concentric oscillatory zoning (Fig. 8a–k). These concordant data allowed us to calculate concordia dates (as of Ludwig 1998) for each sample of this group at 326 ± 3 Ma (MCE33), 348 ± 3 Ma (MCE39), 308 ± 3 Ma (MCE42), 339 ± 2 Ma (MCE151), 305 ± 3 Ma (MCE152), 337 ± 3 Ma (MCE181), 346 ± 5 Ma (MCE182), 305 ± 2 Ma (MCE301) and 301 ± 2 Ma (MCE315) (see Table 1 and Supplementary material for details). Sample MCE150 yields two Carboniferous clusters at ca. 310 Ma and 332 Ma (Table 1), and sample MCE342 gives a Variscan age at ca. 339 Ma in addition to older concordant clusters (Table 1). Older (> 360 Ma), discordant and a few younger U–Pb dates were mainly obtained in CL bright cores and dark grains without oscillatory zoning, respectively.

In the *FeMgG group*, zircon U–Pb dates also yielded relatively complex populations with several clusters of concordant and discordant dates (Fig. 10d–f). Most FeMgG samples display one main cluster of late Carboniferous U–Pb dates, which allows us to calculate ages at 299 ± 3 Ma (MCE142), 303 ± 2 Ma (MCE167c), 301 ± 3 Ma (MCE168), 317 ± 4 Ma (MCE323v) and 318 ± 3 Ma (JB-20–07) (see Table 1 and Supplementary material for details). Some samples also display populations of Permian U–Pb dates, which commonly form linear trends pointing from one dominant cluster of concordant dates (Fig. 10e). For sample MCE183b, the main U–Pb data cluster yields a Permian age of 274 ± 3 Ma (MCE183b) (Fig. 10f). The U–Pb dates older than 360 Ma were obtained on zircon cores and occasionally form small concordant clusters.

For the Olan quartz syenite (samples JB-19–30 and JB-19–58), all analyses yield U–Pb dates concordant within uncertainty (Fig. 10g), and define statistically robust populations that yield ages at 328 ± 2 Ma and 324 ± 2 Ma, respectively (Table 1). In the Colle-Blanche quartz monzonite (JB-20–11), concordant U–Pb data form several clusters of Neoproterozoic, Ordovician, Devonian–early Carboniferous and late Carboniferous age (Fig. 10h). The three oldest groups do not define statistically consistent U–Pb dates (large intra-group dispersion characterized by very high MSWD), but the younger, Carboniferous group yields an age of 307 ± 3 Ma (Fig. 10h; Table 1).

Fig. 8 Examples of zircon morphologies and CL images for all the dated samples. Same scale for all panels

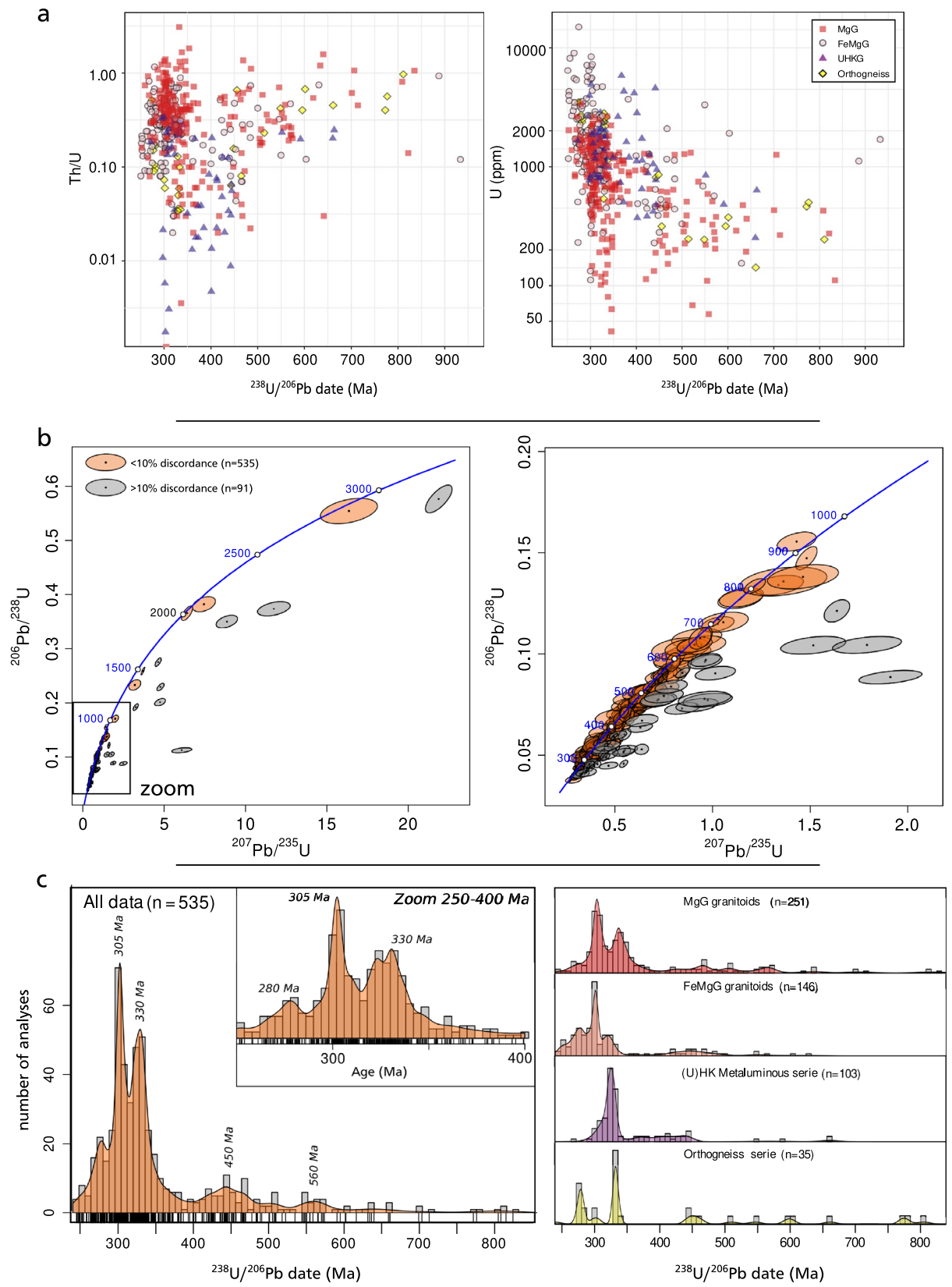

Fig. 9 Summary of U–Pb data. **a** Th/U and U content of dated zircon spots versus $^{238}U/^{206}Pb$ dates. **b** Zircon U–Pb concordia diagrams of all data, and zoomed on dates < 1000 Ma. **c** Histograms and Kernel Density Estimates (KDE) of $^{238}U/^{206}Pb$ dates, for the full dataset and splited by magmatic series

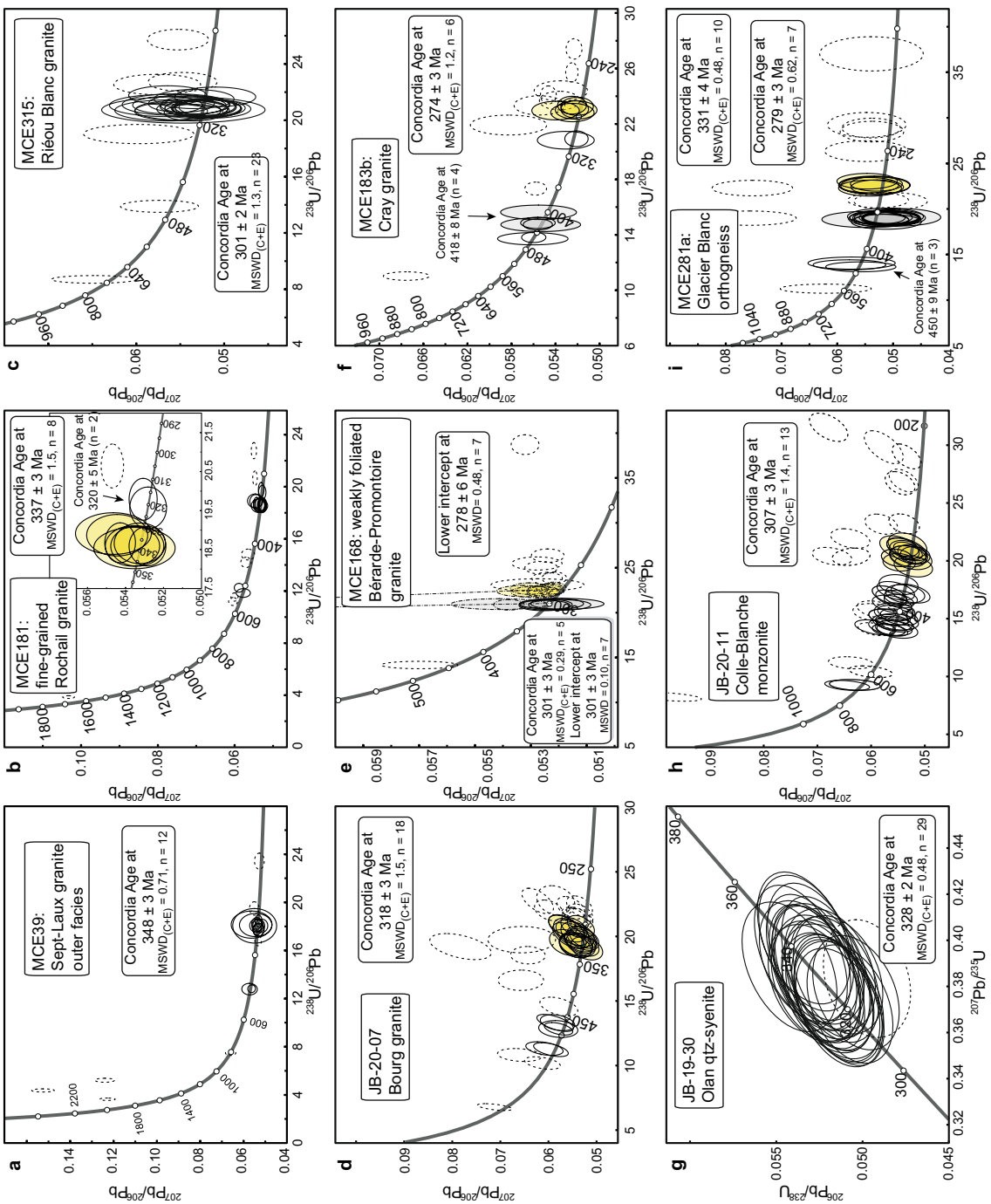

Fig. 10 Representative zircon U–Pb Tera Wasserburg diagrams obtained by LA-ICPMS from MgG samples (**a**–**c**), FeMgG samples (**d**–**f**), UHKM samples (**g**, **h**) and orthogneiss sample (**i**). Other diagrams are available in Online Appendix 1. Error ellipses and uncertainties in ages are ±2σ. Dotted ellipses: points not taken into account for the age calculation

In orthogneisses, U–Pb analyses from sample MCE281a form several concordant clusters at 450 ± 9 Ma, 331 ± 4 Ma and 279 ± 3 Ma (Fig. 10i). Several concordant or sub-concordant analyses yielded Mesozoic dates. MCE324v analyses yielded concordant U–Pb dates spreading from Ordovician to Proterozoic, and numerous discordant data forming two discordia lines with lower intercepts at 592 ± 15 Ma and 468 ± 4 Ma.

Discussion

Interpretation of U–Pb results

Excluding younger outliers presumably related to Pb-loss or other types of isotopic perturbations, most U–Pb data of MgG, FeMgG and UHKM samples yield one or several clusters of concordant Carboniferous to Permian U–Pb dates, with low intra-group dispersion (MSWD = 0.3–1.8). These clusters define Carboniferous ages for most samples, which range from 348 to 299 Ma (Table 1; Fig. 10, Appendix 1), with two exceptions: sample MCE183b (Cray Granite) yielded a main cluster of mid-Permian dates at 274 ± 3 Ma (Fig. 10), and sample MCE281a (orthogneiss) yielded a Permian cluster at 279 ± 3 Ma in addition to a main Carboniferous cluster. These data were obtained on idiomorphic zircon grains with concentric and oscillatory zoning, or on rims also showing concentric zoning. More than 90% of these data are characterized by high Th/U (> 0.1) and high U concentrations (> 200 ppm) (Fig. 9a), suggesting a magmatic origin (Hoskin and Schaltegger 2003; Schaltegger and Davies 2017). Therefore, we interpret the Carboniferous ages as dating the emplacement of the respective intrusive rocks (Table 1). Permian ages are more complex to interpret and are discussed below. Consequently, older concordant U–Pb dates, either isolated or forming clusters, correspond to inherited ages. Some of these older grains exhibit xenocrystic features, such as resorbed grain cores overgrown by magmatic zircon rims (Fig. 8), although there is no clear systematic based on solely CL textures. These inherited ages may reflect either host-rock assimilation during magma ascent or emplacement, or they could have been entrained from the source during crustal melting.

U–Pb analyses on OG samples yield Neoproterozoic and Ordovician dates in sample MCE324v, and Ordovician, Carboniferous and Permian dates in sample MCE281a. Ordovician ages for the orthogneisses in the ECM are widely documented (e.g. Bussy et al. 2011; Vanardois et al. 2022c), and the two OG samples contain large K-feldspar porphyroclasts, which are typical of the Ordovician orthogneisses (see references above). It is quite likely that the two ordovician ages at 450 ± 9 Ma and 468 ± 4 Ma represent the emplacement age of the magmatic protoliths. Therefore, the Neoproterozoic date is an inherited age, and the younger dates are related to posterior (post)-Variscan events.

Pre-Variscan history

Besides the Ordovician zircons, recording the likely protolith age of the Crupillouse and Glacier Blanc orthogneisses, most of the dated samples contain one or several inherited zircon populations. Figure 11 shows the distribution of inherited U–Pb dates with less than 10% discordance from all dated plutonic bodies. This inheritance spectrum is continuous from the Carboniferous to the Neoproterozoic with a main peak at ca. 440 Ma (Fig. 11, KDE area). Several clusters can be recognized at ca. 330 Ma, 370 Ma, 420 Ma, 445 Ma, 505 Ma and 565 Ma (Fig. 11, PDP area).

Early Carboniferous inherited ages observed in the youngest—late Carboniferous—intrusions are inherited from earlier magmatic pulses associated with the emplacement of the older high-K calc-alkaline intrusions, such as the Sept-Laux or Rochail granites. Late Devonian ages are presumably related to the low-K calc-alkaline and tholeitic magmatic activity observed in the southwestern Belledonne and western Pelvoux Massifs (Fréville et al. 2018, 2022).

The main inherited component is Ordovician. It corresponds to prolonged magmatic activity widely documented in the ECM, with numerous intrusions of mafic and felsic magmas dated between ca. 480 and 450 Ma (Bussy et al. 2011; Jacob et al. 2021a, 2022; Rubatto et al. 2010; Schaltegger et al. 2003; Vanardois et al. 2022b, 2022c). It is also consistent with the new dates obtained on the Crupillouse and Glacier Blanc orthogneisses (MCE324v and MCE281a) (Table 1). This magmatic event is extensively documented across the Variscan metamorphic allochthons (Chelle-Michou et al. 2017; Couzinié et al. 2022; García-Arias et al. 2018; Melleton et al. 2010; Soejono et al. 2020; Von Raumer et al. 2015), characterized by the injection of large volumes of felsic and mafic magmas into an extending continental crust, concurrently with the stretching and thinning of the northern Gondwana margin (Von Raumer and Stampfli 2008).

Older clusters can be linked to Pan-African (750–600 Ma) and Cadomian (660–540 Ma) orogenies (Ballèvre et al. 2001; Linnemann et al. 2014). A small number of inherited zircons exhibit pre-Neoproterozoic ages, suggesting potential source regions within internal Gondwana cratons (e.g. Linnemann et al. 2014; Melleton et al. 2010; Stephan et al. 2019). However, considering their scarcity, it is difficult to constrain more precisely the origin of these ancient zircons, whether from the West African craton, the Sahara Metacraton, the Amazonian craton, or the Arabian-Nubian Shield.

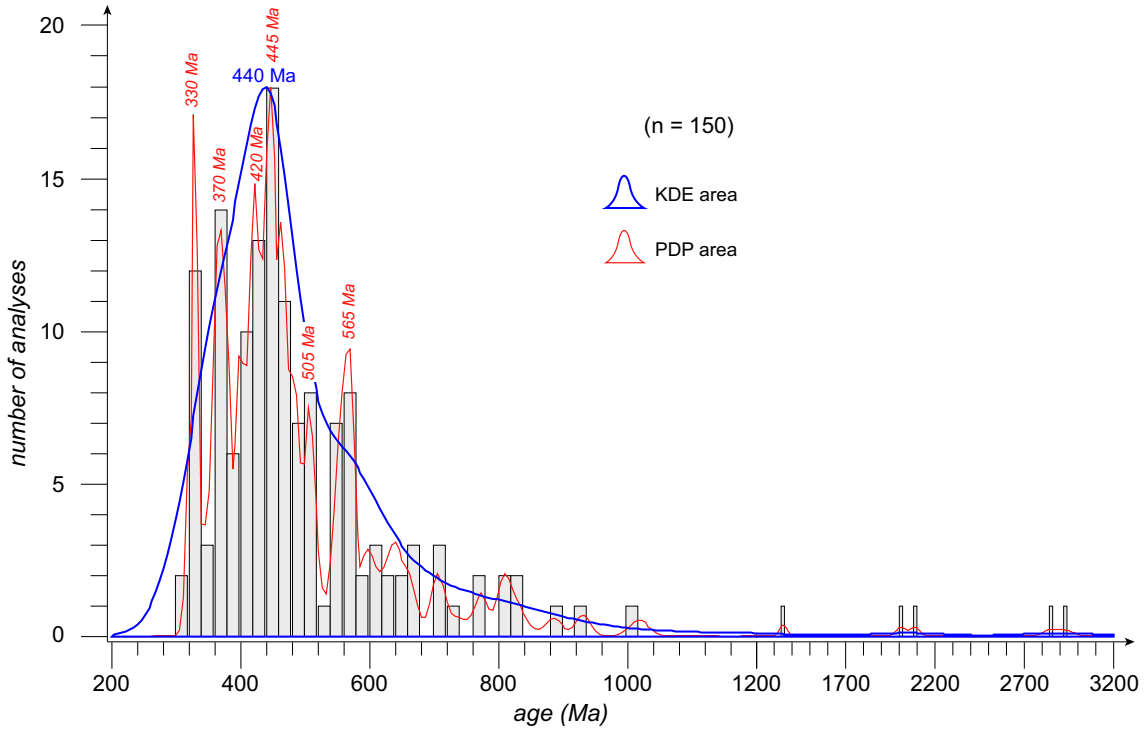

Fig. 11 Histogram, Probability Density Plot (PDP) and Kernel Density Estimates (KDE) of the inherited concordant analyses. See (Vermeesch 2012) for details. Bandwidth = 41.2; bin width = 20

Evidence for a Permian magmatic event

Permian U–Pb dates are observed in many samples, forming a peak in the distribution of U–Pb dates (Fig. 9c), and thus raise the question of a possible post-Variscan magmatic or metamorphic event during the Permian. However, special care must be taken regarding the interpretation of these younger dates, because perturbations related to the Alpine Orogeny are widespread in zircon from the ECM (Gaynor et al. 2022; Ruiz et al. 2022). In several samples, in particular from the Bourg, Bérarde-Promontoire and Etages granites, the younger U–Pb dates typically form linear arrays pointing from one dominant cluster of concordant Variscan U–Pb dates (Fig. 10d, e). This suggests that either Pb-loss or two-component mixing between Variscan and younger—presumably Alpine—zircon has occurred (Gaynor et al. 2022).

However, in the Cray Granite (MCE183b, Fig. 10f) and Glacier Blanc orthogneiss (MCE281a, Fig. 10i), Permian U–Pb dates form concordant clusters clearly separated from older zircon populations, which yield respectively ages of 274 ± 3 Ma (MSWD = 1.2) and 279 ± 3 Ma (MSWD = 0.62). Alpine perturbations have certainly occurred to some extent in these samples, but considering the low dispersion of the zircon populations, it seems very unlikely that the younger ages resulted only from such perturbations. Thus, these two ages likely indicate the existence of an early Permian event in the ECM. For the Cray Granite, the age at 274 ± 3 Ma is interpreted to date the emplacement of the pluton. In the Glacier Blanc orthogneiss, the youngest Permian age of 279 ± 3 Ma is very close to the emplacement age of the Cray granite. However, the emplacement age of this magmatic body is certainly older, since it features high-T deformation, which is inconsistent with a late emplacement after the peak of Variscan tectonic activity and metamorphism. This young age might correspond to new zircon growth or recrystallization triggered by percolating melts or fluids associated with the magmatic event during which the Cray granite was emplaced.

Permian magmatic rocks associated with a HT–LP metamorphism are widespread in the Variscan basement of the Internal Western and Central Alps (Ballèvre et al. 2018; Galli et al. 2011; Kunz et al. 2018), but were so far unknown in the ECM (Ballèvre et al. 2018). This event is generally attributed to crustal thinning of Pangea, representing the premises of continental breakup and opening of the Alpine Tethys (Schuster and Stüwe 2008). The ECM may have been marginally affected by this event, which was more widespread further east in the Briançonnais Domain (Ballèvre et al. 2018 2020). However, more comprehensive geochronological data are needed to constrain more precisely the timing and extent of this HT episode in the ECM.

Magma genesis and evolution

Two contrasted magmatic sources

The clear gap observed between the high-K calc-alkaline granitoids and the durbachites, especially in the B–A and B-Mg# plots (Fig. 5b, f) strongly suggests that two contrasted sources were involved: on the one hand, the mafic to intermediate, ultra-high-K metaluminous durbachites were likely derived from an enriched mantle source. On the other hand, high-K calc-alkaline, peraluminous granitoids (both MgG and FeMgG) all plot close to the granite near-minimum composition (NMC) and were likely generated dominantly by direct melting of crustal protoliths.

However, both the durbachite and high-K calc-alkaline series display significant internal scatter, due to additional petrogenetic processes that operated from the source of magma to its emplacement. Moreover, zircon U–Pb dating clearly shows that the two series were emplaced concomitantly, and thus interactions between these two sources are unavoidable.

The UHKM series (durbachites)

The durbachites display high Ni and Cr content and contain a significant proportion of mafic samples (Figs. 5 and 6), clearly indicating derivation from a mantle source, as concluded by most studies on similar rocks in other Variscan massifs (e.g. Couzinié et al. 2016; Janoušek and Holub 2007; Tabaud et al. 2015). However, the large variability of SiO_2 contents indicates significant evolution from a primary mantle melt, especially in the largest plutonic formations (Olan, Colle-Blanche, Lauzière), where SiO_2 content goes up to ca. 65 wt%. SiO_2-enrichment could have resulted either from direct fractionation of basic mantle melts, re-melting of previously emplaced mafic durbachites, assimilation of felsic crust, mixing with crustal magmas, or a combination of these processes (Annen et al. 2006).

Petrographic differences between plutons suggest that contrasting petrogenetic processes were involved. This emerges clearly when comparing the Colle-Blanche and Olan intrusions. The former is a very heterogeneous plutonic complex, with a large variety of plutonic facies ranging from monzonites to leucogranites (Debon and Lemmet 1999), and contains large amounts of inherited zircon grains of various ages (Fig. 10h)—obvious xenocrysts from the crust. In contrast, the Olan quartz syenites are much more homogeneous and are mostly devoid of inherited zircon (Fig. 10g). Zircon saturation temperatures are close (ca. 780 °C for the Colle-Blanche sample, ca. 840 °C for the Olan samples, Table 2), and both plutons emplaced in similar protoliths. Hence, the observed difference in terms of inherited zircon content likely reflects the difference in magma temperature. The absence of inherited zircon in the Olan quartz-syenite is indicative of high magma temperature well above zircon saturation T (ca. 840 °C), and possibly exceeding 1000 °C considering the presence of stable clinopyroxene in some samples. This temperature significantly surpasses metamorphic conditions locally recorded in the anatectic crust (< 850 °C, Jacob et al. 2022). Consequently, the petrogenesis of these rocks likely involved direct fractionation from hot mantle melts, possibly coupled with the assimilation of crustal components (Bohrson and Spera 2001; DePaolo 1981) or mixing with crustal melts.

Conversely, in the Colle-Blanche Plutonic Complex, the peak temperature either remained below zircon saturation T (ca. 780 °C), or was not sustained long enough to achieve the complete dissolution of zircon in the melt. Such low temperature could be explained by partial melting in the lower crust at ambient metamorphic conditions, including re-melting of already solidified, underplated ultrapotassic mafic magmas together with surrounding crustal lithologies to produce the observed durbachitic (high Mg–K, LILE-LREE-rich) composition. A second option involves mixing or assimilation of crustal leucogranitic melts in mantle-derived, fractionated melts during a late stage of differentiation when the mantle-derived magma had already cooled down too much to dissolve additional zircon. In any case, the combination of a durbachitic composition and abundance of inherited—crustally derived—zircon attests to the very hybrid nature of the Colle-Blanche Plutonic Complex, which contrasts with the more dominantly mantle-derived Olan quartz-syenite.

Strong enrichment in LILE, LREE, U, and Th, as well as highly radiogenic Sr and unradiogenic Nd isotopic signatures are unlikely to have resulted from interactions in the local crust, but reflect instead melting of a LILE–LREE-rich, isotopically mature mantle source with a "crustal" isotopic signature, as already established by numerous studies of durbachites across the Variscan Belt (Couzinié et al. 2016; Hora et al. 2021; Janoušek et al. 2019, 2020; Janoušek and Holub 2007; Laurent et al. 2017; Soder and Romer 2018). The durbachites in our dataset display more radiogenic Sr, and incompatible-element enrichment up to five times higher than the surrounding high-K calc-alkaline granitoids (Fig. 6), suggesting that the enriched mantle source is richer in lithophile elements and more isotopically-mature than the local anatectic crust in the ECM.

Relationship with mantle metasomatic processes has been furthermore established by the study of mantle eclogites, garnet clinopyroxenites and peridotites enclaves incorporated in the deep orogenic root, which shows clear evidence of interactions with silicic, LILE–LREE-rich fluids or melts derived from subducted Variscan continental crust or sediments (Becker 1996; Borghini et al. 2018, 2023; Medaris et al. 2015; Scambelluri et al. 2006). In the ECM, similar processes have been recently documented in peridotite

enclaves embedded in lower crustal migmatites from the Pelvoux Massif (Jacob et al. 2023), validating the connection between the local durbachites and melting of a metasomatized mantle source.

The high-K calc-alkaline granitoids (MgG and FeMgG)

The high-K calc-alkaline granitoids form a relatively homogeneous group, of acidic ($SiO_2 > 63$ wt%) and peraluminous rocks (Fig. 5), without mafic or intermediate members, and containing variable proportions of inherited zircon. All these characteristics are in line with a predominance of crustal source(s). However, the crustal protoliths possibly involved could be very diverse, including felsic orthogneiss, aluminous metasediments, mafic–intermediate low-K volcanosediments and low-K tholeiitic metabasalts (Barféty and Pêcher 1984; Guillot and Ménot 2009; Le Fort 1971). Furthermore, considering the close connection with the durbachites in the field, it is almost certain that interaction with ultra-high-K mantle-derived melts occurred. This complex petrogenesis can be broadly discussed within a simplified framework involving three main magma sources: felsic high-K crustal rocks, mafic low-K crustal rocks, and enriched mantle. The compositional variability observed between different intrusions would thus result primarily from interaction, in variable proportions, between magmas derived from these three sources (magma mixing, assimilation of host rocks and/or mafic enclaves, etc.), in addition to closed-system fractional crystallization. Source contributions can be assessed in the ternary diagram A/CNK—Na_2O/K_2O—FMSB ([FeO + MgO] × [Ba + Sr]) of Laurent et al. (2014a, b) (Fig. 12). It was originally designed to discriminate Archean sodic TTG series from Mg–K-rich mantle-derived magmas (sanukitoids), but it also performs relatively well to discriminate Variscan igneous suites (Laurent et al. 2017). A clear gap is observed with the durbachites, which plot in the "LILE-rich mantle" field, while the high-K calc-alkaline granitoids predominantly require a high-K felsic and low-K mafic crustal parentage. Small variations in Na_2O/K_2O are observed (Figs. 5d and 12), which may reflect variable contributions of low-K mafic and high-K felsic sources. In particular, this could explain the slightly more sodic composition of the MgG compared to the FeMgG (Fig. 5d). Indeed, the former are predominantly located in the western part of the ECM, where the metamorphic pile contains a large proportion of low-K mafic protoliths, while the latter are more concentrated in the eastern part, where high-K felsic protoliths dominate (Fig. 2). However, the low-K mafic pole always remains a subordinate component in the source of the high K calc-alkaline granitoids. They nearly all plot in the field corresponding to dominant high-K felsic sources, with very few compositions in the "low-K mafic" field.

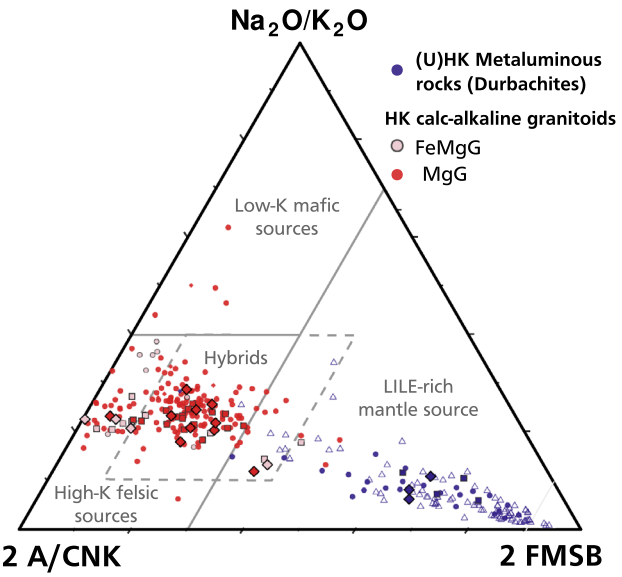

Fig. 12 Ternary discrimination diagram of Laurent et al. (2014a, b), based on late-Archean granitoid typology (FMSB = [FeOt + MgO] wt% × [Sr + Ba]wt%). Color and symbol code from Fig. 5

Dispersion toward the "LILE-rich mantle" apex reflects the high LILE content of some granitoids, especially in the MgG group (Fig. 6), reflecting interactions with LILE–LREE-rich mantle-derived magmas and their derivatives. Evidence of these interactions is observed in the field. Many mafic durbachite enclaves in granitoids show darker rims enriched in mafic minerals (biotite, amphibole), which suggests a reaction between the enclaves and the granitic melt (Fig. 4b). Clusters of dark minerals observed in the granite also indicate mineral entrainment from these enclaves into the melt. Detailed geochemical investigations of the enclave–host pairs in the Sept-Laux, St-Colomban, and Lauzière Plutons by Debon et al. (1998) also led to the conclusion that intimate interactions have occurred between the enclaves and the host.

Thus, the high-K calc-alkaline granitoids were probably derived predominantly from the melting of felsic crustal sources, with a subordinate role for the mafic crust and hybridization with LILE–LREE-rich durbachite melts derived from the enriched mantle. Such hybridization had limited effect on the major-element chemistry of granitoids, as shown by the clear gap between granitoids and durbachites on compositional diagrams (esp. Figures 5a, b, f and 12). However, enriched mantle-derived melts may have represented a much more significant contribution to the trace-element budget, in particular of LILE, LREE, and some HFSE (U, Th) (Couzinié et al. 2016).

Temporal evolution of granitoid compositions

Major and trace elements

Geochemistry of the ECM granitoids evolved with their emplacement ages. To highlight this correlation, we grouped geochemical data by plutonic formation and assigned them an age taken from our U–Pb dating or from literature (Cannic 1998; Debon et al. 1998; Guerrot and Debon 2000). Mafic enclaves and data from undated plutonic formations were removed. Median compositions and interquartile ranges in each dated pluton are shown as a function of emplacement age. Besides this illustrative set of whole-rock geochemical parameters (Fig. 13), including Nd isotopes (Fig. 14), a more comprehensive set of plots is available in the electronic supplements (Fig. S2).

A gradual decrease in median Mg# of high-K calc-alkaline granitoids over time is observed (Fig. 13a). This trend was previously noticed by Debon and Lemmet (1999), who categorized Variscan ECM granitoids into an older (Visean), high Mg# suite and a younger (Stephanian) low Mg# suite. However, with our expanded geochronological dataset, it becomes clear that this transition from high-Mg# to low-Mg# compositions occurred smoothly, without any clear gap between the older and younger intrusions. Therefore, variations in Mg# represent the progressive evolution of a single magmatic suite rather than two distinct magmatic series.

A notable increase in median SiO_2, and a concurrent decrease in median Sr/Y and La/Yb over time are observed (Fig. 13b–d), corresponding to an increase in HREE + Y correlated with a decrease in Sr. Median Nb and Ta contents both increase, but Nb/Ta decreases over time, as well as Th/Nb (Fig. 13e–f). In contrast, no particular trend is observed for other LILE (Rb, Ba), LREE, nor for Th and U (Fig. S2). This evolution is consistent with an increased fractionation of magmas over time, which tends to decrease Mg# (Debon and Le Fort 1988), Sr/Y and La/Yb (Moyen 2009) as well as Nb/Ta (Linnen and Keppler 1997) in the residual melt. However, no significant variations of Rb and Ba are observed, which would be expected with increasing fractionation of the melt. Moreover, equally-differentiated compositions with similar maficity

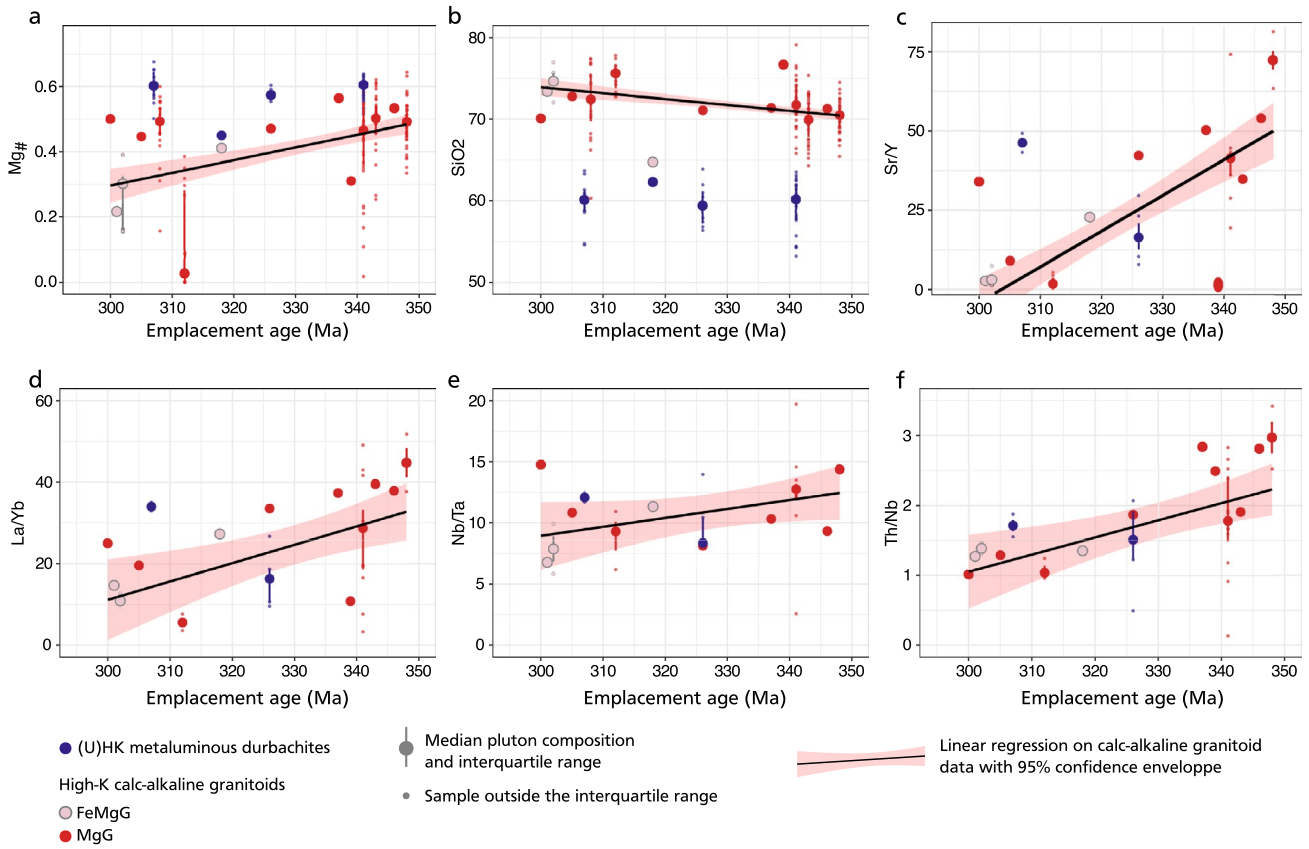

Fig. 13 Median compositions of plutons versus their age of emplacement for a chosen set of geochemical parameters. Additional plots are provided in the electronic supplements, or can be computed using the R-code and the data also provided. Linear regression models (black line) have been computed using data from the MgG and FeMgG groups only. Red-shaded areas represent the 95% confidence interval on each regression

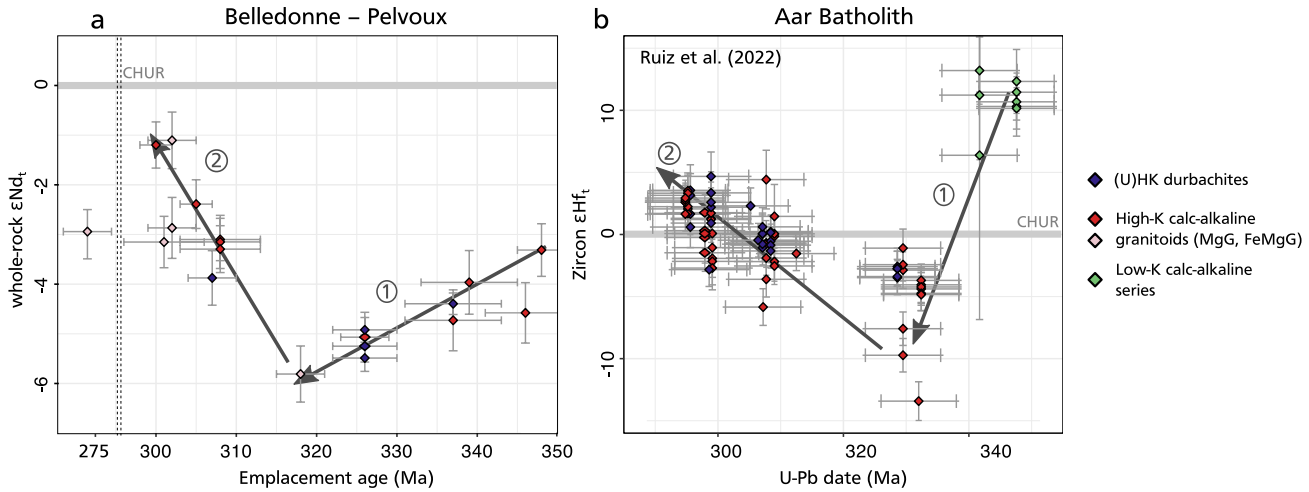

Fig. 14 **a** Initial Nd isotopic compositions (εNd_i) versus U–Pb emplacement age for samples from the Belledonne—Pelvoux Massifs (this study). **b** Zircon εHf_i data from Ruiz et al. (2022) on plutonic formations from the Aar Batholith (northern ECM), showing the same trends: (1) decreasing εNd_i from ca. 345 to 330–320 Ma, (2) increasing εNd_i from 330–320 to 300–300 Ma. No distinction is made between the FeMgG and MgG sub-series in the Aar Batholith, and high-K calc-alkaline granitoids are indistinctively plotted in red

(B) can display a large range of Mg# (Fig. 5f), which indicates that besides fractionation, additional processes were involved.

These additional processes might include an evolution of source composition, crustal versus mantle sources mass-balance, or melting P–T conditions.

The progressive decrease in Sr/Y, La/Yb and Nb/Ta ratios is consistent with a progressive decrease of melting pressure in the crust. In older granitoids (Visean), higher Sr/Y, La/Yb and Nb/Ta ratios could signify deep melting or fractionation in equilibrium with garnet–rutile-rich and plagioclase-poor residues/cumulates (Profeta et al. 2015; Sundell et al. 2021). The progressive decrease of these ratios over time would reflect destabilization of the garnet + rutile assemblages, in relation with a progressive decrease in melting pressure. This evolution could be related either to the propagation of the melting region toward the shallower crust, or to progressive thinning of the lithosphere associated with the post-orogenic collapse. This evolution is consistent with the P–T–t evolution of metamorphic rocks from the ECM, which record peak-P conditions (up to ca. 1.5 GPa) during the Visean (ca. 340 Ma), followed by progressive decompression down to ca. 0.6 GPa during the late Carboniferous associated with a destabilization of garnet–rutile assemblages and melting of both mafic and felsic protoliths in the garnet-absent field (Fréville et al. 2022; Grandjean et al. 1996; Jacob et al. 2022).

Besides that, the same trends could result from an evolution of source composition, or from a changing balance between crustal and mantle sources. In particular, a decreasing contribution of the LILE-rich mantle source, characterized by high Mg# as well as elevated Sr/Y and La/Yb would be consistent with field observations: older plutons with high Mg#, Sr/Y and La/Yb are richer in mantle-derived durbachite enclaves compared to the younger granitoids (Fig. 4), which suggests a larger degree of hybridization with enriched mantle-derived melts in the former. A progressive decrease of Sr/Y and La/Yb in the mantle source at constant mantle contribution would also produce a similar effect, however.

Hence, the observed geochemical variations probably resulted from a combination of different effects, including variations of the mantle/crustal source compositions, their proportions, decreasing melting pressure, and increasing degree of fractionation of magmas over time (Fig. 15). However, deciphering the respective contributions of each mechanism in the general trends observed on Fig. 13 remains a challenge.

Neodymium isotopes

The Nd isotopic compositions recalculated at the time of emplacement (εNd_i) also reveal a significant evolution with time (Fig. 14a). The εNd_i values of dated granitoids and durbachites decrease from ca. [−3.8; −2.8] to ca. [−6.4; −5.2] between 345 and 320 Ma, and then increase back to ca. [−3.7; −0.5] in the late Carboniferous intrusions (ca. 300 Ma). This evolution is observed both in the high-K calc-alkaline granitoids (FeMgG and MgG) and in the UHKM series, whose εNd_i overlap for the same emplacement age. Nd isotopic composition of the Cray granite (274 ± 3 Ma) is similar to that of the late Carboniferous group ($\varepsilon Nd_i = -3.0$). Strontium isotopes do not show any

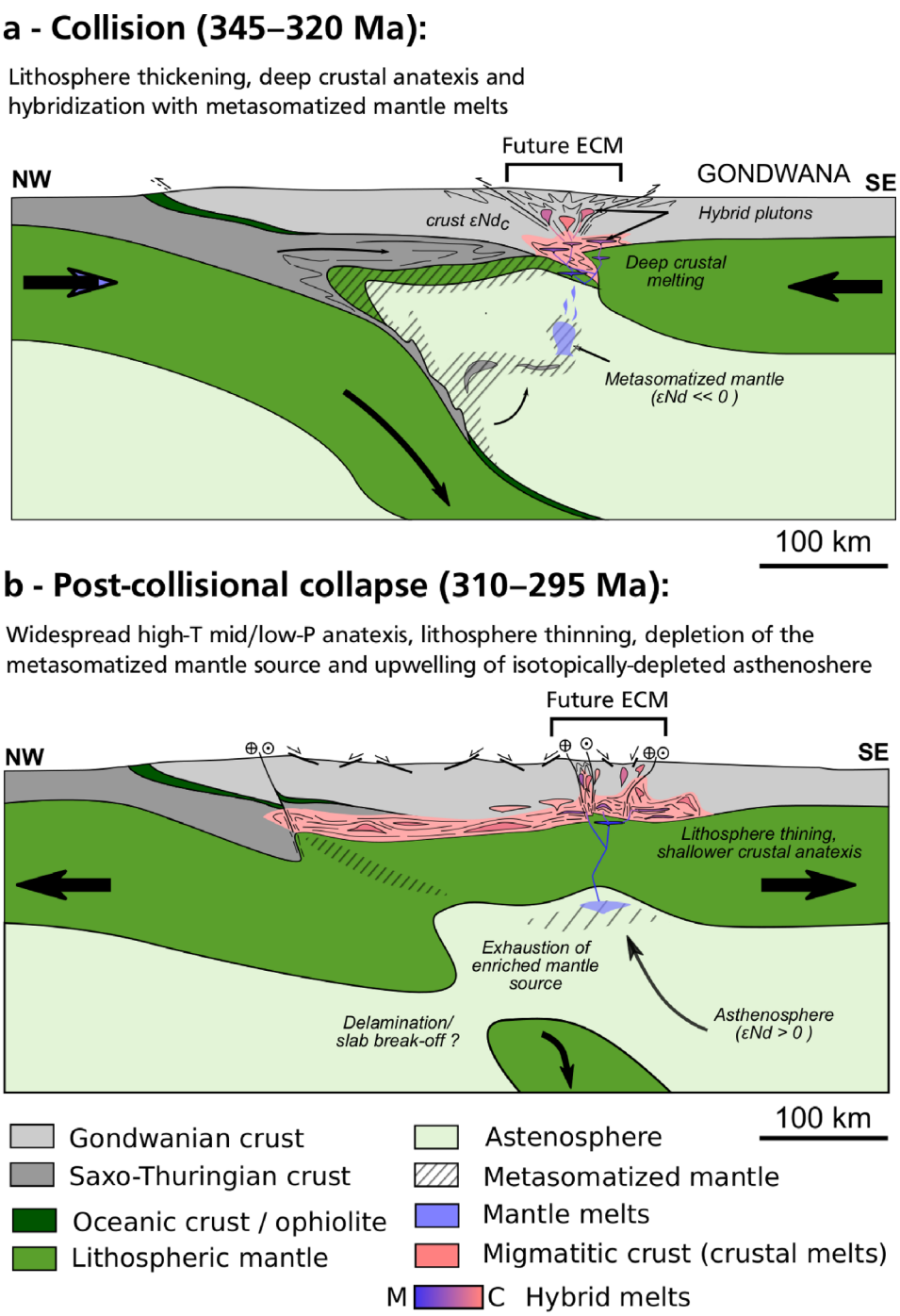

Fig. 15 Possible geodynamic scenario along the central-eastern segment of the Variscan Belt, which may account for the temporal evolution of magmatism in the External Crystalline Massifs. **a** Continental subduction/collision with crustal thickening and incorporation of mature crustal material in the mantle wedge. **b** Progressive orogenic collapse, associated with lithospheric thinning, increased anatexis and involvement of a more depleted mantle in the source of mafic magmas

particular trend. Considering Rb is prone to leaching by metamorphic fluids (Harlov and Austrheim 2013), the Sr isotopic composition may have been significantly altered, and is, therefore, not discussed. The εNd_i evolution is very similar to the trend recorded by zircon Hf isotopes in the Aar Batholith (Fig. 14b, Ruiz et al. 2022), which shows a progressive decrease in εHf_i from [+10; +12] at ca. 348 Ma to [−10; −3] at ca. 333 Ma, followed by an increase to [−3; +6] in zircon from late Carboniferous pulses (ca. 309 and 298 Ma), both in high-K calc-alkaline granitoids and durbachites. Highly radiogenic values ($\varepsilon Nd_i > +10$) reported in lower Carboniferous intrusions (Fig. 14b) correspond mainly to diorites and tonalites akin to the pre/early collisional low-K calc-alkaline series.

Thus, the observed evolution of Nd-Hf isotopes is consistent throughout the ECM. It may reflect either variations of the relative contribution of crustal and mantle melts at constant source composition, or variations of the isotopic composition of crustal and/or mantle sources at constant mass balance. Both mechanisms seem plausible, but a scenario

involving primarily mass-balance shifts seems difficult to support, mainly because the isotopic evolution of high-K calc-alkaline granitoids and durbachites are highly correlated (Fig. 14), despite very contrasted contributions of the crust and the mantle in these two series. Thus, an evolution of the isotopic composition of either the mantle or crustal sources, or both, is required to explain the observed trends.

The ECM crust is highly heterogeneous. Isotopic data on pre-Carboniferous crustal protoliths are scarce, but by comparison with other Variscan Massifs (e.g., French Massif Central, Chelle-Michou et al. 2017; Downes et al. 1990; Simien et al. 1999), variations of bulk rock εNd_i from −10 to +8 depending on rock type is realistic and can potentially explain the εNd_i variability in the granitoids, if the distribution of protoliths involved in anatexis evolved over time. However, this does not explain correlated variations between the durbachites and the granitoids. Furthermore, the increase of εNd_i and εHf_i observed toward CHUR value during the late Carboniferous would more probably involve an increased contribution of low-K mafic protoliths (εNd_i between +6 and +8, Paquette et al. 1989). These rocks are not particularly enriched in Nd compared to the granitoids/felsic protoliths (Paquette et al. 1989), and thus a significant amount of this material would be required to shift the isotopic composition of the late-Carboniferous granitoids close to CHUR values. This should be reflected in the bulk rock composition of the granitoids, in particular in K/Na, which is not observed (Fig. S5, electronic supplements). Variations of the isotopic composition of crustal melts over time remain possible, but it seems unlikely that it is the main driver of the trends observed on Fig. 14.

In our view, isotopic variations in the mantle source represent a significant contribution to the observed trends. The mantle isotopic composition can vary within a broad range, from depleted mantle values ($\varepsilon Nd_i \sim +9$, Salters and Stracke 2004) to isotopically-mature, highly metasomatized mantle (εNd_i from −5 to −10, Janoušek et al. 2022), covering the full range of observed εNd_i, providing a direct explanation to the variations in the durbachites. Correlation between isotopic variations in the mantle and in the high-K calc-alkaline granitoids is however not straightforward, since the latter are dominantly crustally derived. However, the Nd mass-balance in this series is certainly more shifted toward the mantle pole than the total mass-balance, because mantle-derived melts are much more enriched in Nd than the crustal melts. A rough mass-balance calculation assuming Nd content of 90–130 ppm in the primitive mantle melts (Nd-content of the most mafic durbachites in our dataset), 10–20 ppm in the crustal protoliths (a realistic value regarding the distribution of Nd-content of granitoids in our dataset), and 10 to 20% mantle contribution in the high-K calc-alkaline series, indicates that the mantle contribution to the Nd budget of the granitoids realistically lies between 35 and 75%. Such a contribution is large enough to produce a significant shift in the Nd isotopic composition of the granitoids if the isotopic composition of the mantle source shifts over time.

In this scenario, the εNd_i decrease from 345 to 320 Ma (Fig. 14) would mark progressive isotopic enrichment of the mantle source, by incorporation of deeply subducted, isotopically-mature crustal material (Fig. 15a). possibly related to sub-lithospheric relamination (Maierová et al. 2021; Schulmann et al. 2014).

The εNd_i increase during the late Carboniferous would mark a return to more radiogenic Nd isotopic composition in the mantle, either due to depletion of the enriched mantle lithosphere by protracted melt extraction during the Carboniferous, or by advection of isotopically depleted asthenosphere, or both (Fig. 15b). Asthenospheric upwelling could have resulted, for instance, from thinning of the lithospheric mantle, lithosphere delamination or slab breakoff, scenarios that have been commonly proposed for the late stages of the Variscan Orogeny (e.g. Faure et al. 2009; Lardeaux et al. 2014; Vanderhaeghe et al. 2020). Progressive return to less enriched mantle with more radiogenic Nd-Hf isotopes is also consistent with the broader magmatic evolution observed in the Paleozoic basement of the Western Alps. In particular, the geochemistry and isotopic composition of younger Permian magmatic series, especially in the Briançonnais zone (Ballèvre et al. 2020) and the Ivrea zone (e.g. Storck et al. 2021) also indicate a decreasing isotopic enrichment of the mantle source toward the late Paleozoic.

Timing of magmatism

The new geochronological results show that magmatic activity was not restrained to two large episodes at ca. 340 Ma and 300 Ma, as previously stated (Debon and Lemmet 1999). Even though increased magmatic activity occurred during these two periods, multiple plutonic intrusions were emplaced in between, such as the Bourg granite at 318 ± 3 Ma or the Olan quartz syenite at 324 ± 2 Ma (Fig. 16). Variable ages obtained within the same pluton (e.g. Sept-Laux granite: 348 ± 3 and 326 ± 3 Ma; Rochail granite: 346 ± 5 and 337 ± 3 Ma) indicates incremental growth during several magmatic episodes separated by several millions of years. However, deciphering the precise timing of incremental magmatic events is out of reach with the age resolution of LA-ICPMS data. Higher resolution ID-TIMS dating with precision < 1% (Parrish et al. 2003) would be needed for this purpose. This result is in line with data from Ruiz et al. (2022), in the Aar Batholith, the largest plutonic complex of the ECM (Fig. 1), which was built incrementally by several magmatic episodes at ca. 348, 333, 309 and 298 Ma.

Thus, Variscan magmatism in the ECM was less discontinuous than previously thought. This implies that large portions of the Variscan lower to middle crust and lithospheric

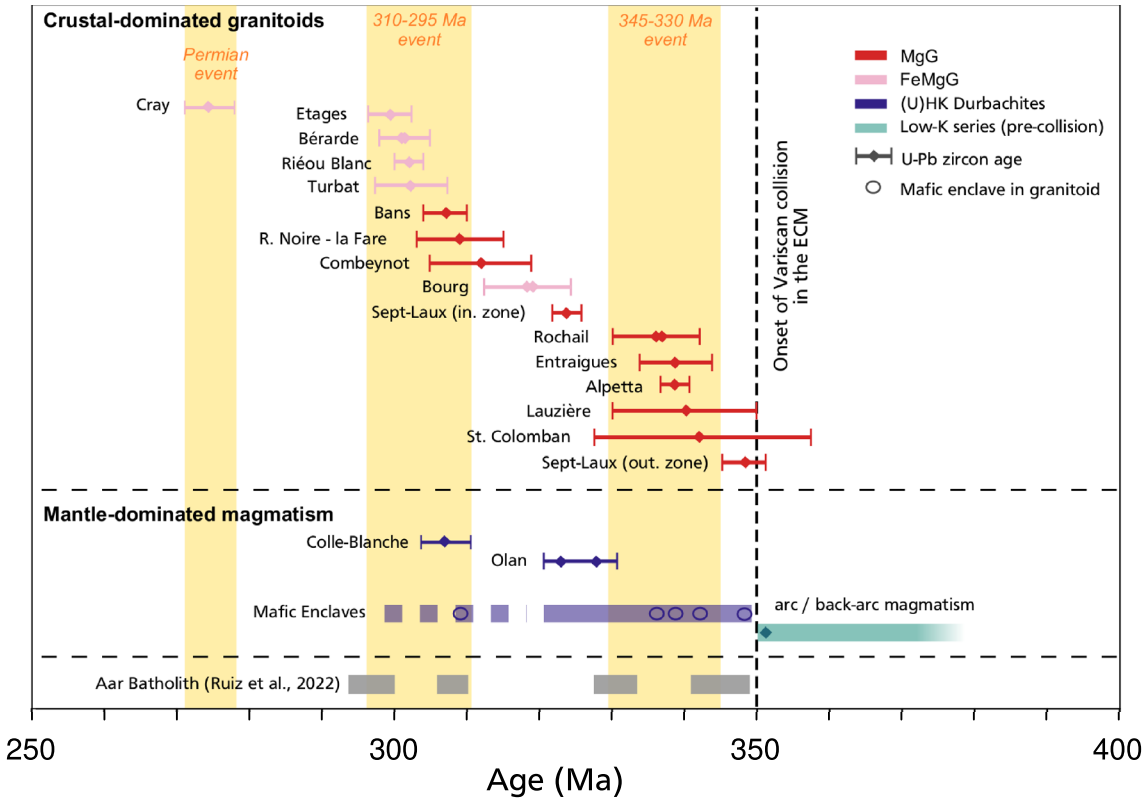

Fig. 16 Summary of pluton emplacement ages in the central ECM, using data from this study and from previous dating work (Debon et al. 1998; Fréville et al. 2018). Plutons are separated between crustal-dominated series (FeMgG and MgG) and mantle-dominated series (UHKM, and the low-K calc-alkaline and tholeiitic pre-collisional magmas). Data from the Aar Batholith (Ruiz et al. 2022) have been added for comparison

mantle were prone to melting for a protracted period, from the early Visean to the earliest Permian (ca. 350–295 Ma). This is confirmed by petrochronological data on metamorphic rocks, which show that metamorphic conditions close to, or higher than the wet granite solidus (ca. 0.5–1.0 GPa, 550–700 °C) were reached in the middle crust already from the Visean (ca. 340–335 Ma), and then further increased, reaching locally granulite-facies conditions (ca. 800–850 °C, 0.6–0.9 GPa) during the late Carboniferous (Ferrando et al. 2008; Fréville et al. 2022; Guillot and Menot 1999; Rubatto et al. 2010; Vanardois et al. 2022b).

This general increase in crustal temperature during the Carboniferous was reflected in the magmatic productivity. Indeed, most of the largest granitoid intrusions in the ECM, such as the Central Aar granite (ca. 500 km^2, ca. 298 Ma, Ruiz et al. 2022), the Mont-Blanc granite (280 km^2, ca. 305 Ma, Bussy et al. 2000, Vanardois et al. 2022c), or the central Pelvoux granitic complex (Etages, Bérarde-Promontoire and Cray granites: ca. 115 km^2, ca. 301–299 Ma, Fig. 2) were emplaced during the late Carboniferous to earliest Permian, while older granitoids (with the notable exception of the Sept-Laux Pluton in Belledonne) formed generally smaller bodies.

Conclusions

The available geochronological, geochemical and isotopic data, both new and compiled from literature, provide new constraints on the timing and petrogenesis of Variscan magmatism of the External Crystalline Massifs (ECM) during the Carboniferous. Geochronological data highlight a long-lived magmatic activity consisting of two main magmatic episodes during the Visean (ca. 348–335 Ma) and the late Carboniferous (305–299 Ma), with several smaller episodes in between. Thus, this magmatic activity covers most of the Variscan Orogeny in the ECM from the early syn-collisional stages to the post-collisional collapse. An early Permian episode around 275 Ma has also been identified, which can be correlated with Permian magmatism recorded further east in the internal Alpine basement.

Contemporaneous emplacement of two contrasted magmatic series, namely ultra-high-K metaluminous rocks (durbachites) and high-K calc-alkaline peraluminous granitoids (FeMgG and MgG suites), reflects concomitant crustal and enriched mantle melting. However, these two series do not represent pure mantle and crust-derived end-members: significant hybridization occurred, either

by magma mixing or assimilation of crystallized mafic enclaves in the granitoids, as revealed by trace-element compositions and by the presence of inherited zircon grains in nearly all the dated magmatic bodies.

Long-term variations are observed in the geochemical compositions of granitoids, especially a temporal decrease in Mg#, La/Yb and Sr/Y and increase in SiO_2. These variations probably arise from a combination of several mechanisms, including changes in the balance of felsic crust, mafic crust, and mantle in the source of granitoids, mantle-source variability and progressive decrease in melting pressure from the early syn-collisional to the post-collisional stages. The εNd_i values also show variations with time, which are similar in the durbachites and the high-K calc-alkaline granitoids, and partly result from an evolution of the mantle source isotopic composition during the orogeny, probably in addition to an increased contribution of crustal melting over time, in particular from low-K mafic protoliths with a radiogenic Nd isotopic composition. The εNd decrease from ca. 345 to 320 Ma might reflect an increasing influence of deeply subducted/relaminated crustal material contaminating the lithospheric mantle source. Then, a return to a more depleted Nd isotopic composition toward the late Carboniferous might be either due to the progressive depletion of the enriched mantle by protracted melt extraction, or due to advection of non-metasomatized asthenosphere with a more radiogenic Nd composition.

Supplementary Information The online version contains supplementary material available at https://doi.org/10.1007/s00531-024-02420-y.

Acknowledgements This work was supported by the French RENATECH network, and by the bureau de Recherches Géologiques et Minières (BRGM) through the "RGF Alpes and peripheral basins" project. We greatly thank Ulrich Riller for editorial handling, as well as Vojtěch Janoušek and Simon Couzinié for taking the time and effort to review the manuscript.

Funding Open access funding provided by University of Oslo (incl Oslo University Hospital).

Data availability Data supporting this research are available in the electronic supplementary material, in addition with the R code for processing whole-rock geochemical data.

Declarations

Conflict of interest The authors declare that they have no competing financial interests or personal relationships that could have appeared to influence the work reported in this paper.

References

Annen C, Blundy JD, Sparks RSJ (2006) The genesis of intermediate and silicic magmas in deep crustal hot zones. J Petrol 47:505–539. https://doi.org/10.1093/petrology/egi084

Aumaitre PR, Giraud P, Poncerry E, Vivier G (1985) Les granitoïdes subalcalins potassiques de la Lauzière, Massif Cristallin Externe de Belledonne (Alpes Françaises). Géol Alpine 61:17–32

Ballèvre M, Le Goff E, Hébert R (2001) The tectonothermal evolution of the Cadomian belt of northern Brittany, France: a Neoproterozoic volcanic arc. Tectonophysics 331:19–43. https://doi.org/10.1016/S0040-1951(00)00234-1

Ballèvre M, Manzotti P, Piaz GVD (2018) Pre-alpine (Variscan) inheritance: a key for the location of the future Valaisan basin (Western Alps). Tectonics 37:786–817. https://doi.org/10.1002/2017TC004633

Ballèvre M, Camonin A, Manzotti P, Poujol M (2020) A step towards unraveling the paleogeographic attribution of pre-Mesozoic basement complexes in the Western Alps based on U–Pb geochronology of Permian magmatism. Swiss J Geosci 113:12. https://doi.org/10.1186/s00015-020-00367-1

Banzet G (1987) Interaction croûte-manteaux et genese du plutonisme subalcalin du Haut Dauphiné occidental (Massifs cristallins externs): Vaugnérites, durbachites et granitoides magnésio-potassiques. Géol Alpine 63:95–117

Barbarin B (1999) A review of the relationships between granitoid types, their origins and their geodynamic environments. Lithos 46:605–626. https://doi.org/10.1016/S0024-4937(98)00085-1

Barféty JC, Pêcher A (1984) Geological map and explanatory text of the sheet n 822 "St Christophe en Oisans", scale: 1: 50000, BRGM ed

Becker H (1996) Geochemistry of garnet peridotite massifs from lower Austria and the composition of deep lithosphere beneath a Palaeozoic convergent plate margin. Chem Geol 134:49–65. https://doi.org/10.1016/S0009-2541(96)00089-7

Bellanger M, Augier R, Bellahsen N, Jolivet L, Monié P, Baudin T, Beyssac O (2015) Shortening of the European Dauphinois margin (Oisans Massif, Western Alps): new insights from RSCM maximum temperature estimates and 40Ar/39Ar in situ dating. J Geodyn 83:37–64. https://doi.org/10.1016/j.jog.2014.09.004

Boehnke P, Watson EB, Trail D, Harrison TM, Schmitt AK (2013) Zircon saturation re-revisited. Chem Geol 351:324–334

Bohrson WA, Spera FJ (2001) Energy-constrained open-system magmatic processes II: application of energy-constrained assimilation–fractional crystallization (EC-AFC) model to magmatic systems. J Petrol 42:1019–1041

Bordet P, Bordet C (1963) Belledonne-Grandes Rousses et Aiguilles Rouges-Mont Blanc: quelques données nouvelles sur leurs rapports structuraux. Mém H.s Soc Géol Fr 2:309–316

Borghini A, Ferrero S, Wunder B, Laurent O, O'Brien PJ, Ziemann MA (2018) Granitoid melt inclusions in orogenic peridotite and the origin of garnet clinopyroxenite. Geology 46(11):1007–1010. https://doi.org/10.1130/G45316.1

Borghini A, Nicoli G, Ferrero S, O'Brien PJ, Laurent O, Remusat L, Borghini G, Milani S (2023) The role of continental subduction in mantle metasomatism and carbon recycling revealed by melt

inclusions in UHP eclogites. Sci Adv 9:eabp9482. https://doi.org/10.1126/sciadv.abp9482
Bosch D, Bruguier O, Caby R, Buscail F, Hammor D (2016) Orogenic development of the Adrar des Iforas (Tuareg Shield, NE Mali): new geochemical and geochronological data and geodynamic implications. J Geodyn 96:104–130
Bouvier A, Vervoort JD, Patchett PJ (2008) The Lu–Hf and Sm–Nd isotopic composition of CHUR: constraints from unequilibrated chondrites and implications for the bulk composition of terrestrial planets. Earth Planet Sci Lett 273:48–57
Bussien-Grosjean D, Meisser N, May-Leresche S, Ulianov A, Vonlanthen P (2018) The Morcles microgranite (Aiguilles Rouges, Swiss Alps): geochronological and geochemical evidences for a common origin with the Vallorcine intrusion. Swiss J Geosci 111:35–49. https://doi.org/10.1007/s00015-017-0282-3
Bussy F, Hernandez J, Von Raumer J (2000) Bimodal magmatism as a consequence of the post-collisional readjustment of the thickened Variscan continental lithosphere (Aiguilles Rouges-Mont Blanc Massifs, Western Alps). Trans Roy Soc Edinb Earth Sci 91:221–233
Bussy F, Péronnet V, Ulianov A, Epard JL, Raumer J (2011) Ordovician magmatism in the external French Alps: witness of a perigondwanan active continental margin. In: International symposium on the ordovician system (11–2011; Alcalá de Henares, Madrid)
Cannic S, Lapierre H, Schärer U, Monié P, Briqueu L, Basile C (1998) Origin of hercynian magmatism in the French Western Alps: geochemical and geochronological constraints. Min Mag A 62:274–275
Carignan J, Hild P, Mevelle G, Morel J, Yeghicheyan D (2001) Routine analyses of trace elements in geological samples using flow injection and low pressure on-line liquid chromatography coupled to ICP-MS: a study of geochemical reference materials BR, DR-N, UB-N, AN-G and GH. Geostand Newslett 25:187–198. https://doi.org/10.1111/j.1751-908X.2001.tb00595.x
Carme F, Pin C (1987) Vue d'ensemble sur le magmatisme pré-orogénique et l'évolution métamorphique et tectonique varisques dans le sud de la chaîne de Belledonne (Massifs cristallins externes, Alpes françaises). C R Acad Sci II A 304:1177–1181
Chardon D, Aretz M, Roques D (2020) Reappraisal of Variscan tectonics in the southern French Massif Central. Tectonophysics 787:228477. https://doi.org/10.1016/j.tecto.2020.228477
Chelle-Michou C, Laurent O, Moyen J-F, Block S, Paquette J-L, Couzinié S, Gardien V, Vanderhaeghe O, Villaros A, Zeh A (2017) Pre-Cadomian to late-Variscan odyssey of the eastern Massif Central, France: formation of the West European crust in a nutshell. Gondwana Res 46:170–190
Clemens JD (2012) Granitic magmatism, from source to emplacement: a personal view. Appl Earth Sci 121:107–136
Costarella R (1987) Le complexe annulaire alcalin de Combeynot (Massifs cristallins externes, Alpes françaises), témoin d'un magmatisme en régime distensif. Pétrogéochimie et signification géodynamique. Doctoral dissertation, Université Scientifique et Médicale de Grenoble
Couzinié S, Laurent O, Moyen J-F, Zeh A, Bouilhol P, Villaros A (2016) Post-collisional magmatism: crustal growth not identified by zircon Hf–O isotopes. Earth Planet Sci Lett 456:182–195. https://doi.org/10.1016/j.epsl.2016.09.033
Couzinié S, Bouilhol P, Laurent O, Grocolas T, Montel J-M (2022) Cambro-Ordovician ferrosilicic magmatism along the northern Gondwana margin: constraints from the Cézarenque-Joyeuse gneiss complex (French Massif Central). Bull Soc Géol Fr 193:15. https://doi.org/10.1051/bsgf/2022010
De Boisset T (1986) Les enclaves basiques du granite du Rochail (syénite du Lauvitel)—Haut Dauphiné, Alpes françaises. Pétrographie et minéralogie. Doctoral dissertation, Université Scientifique et Médicale de Grenoble
Debon F, Le Fort P (1983) A chemical–mineralogical classification of common plutonic rocks and associations. Trans Roy Soc Edinb Earth Sci 73:135–149. https://doi.org/10.1017/S0263593300010117
Debon F, Lemmet M (1999) Evolution of Mg/Fe ratios in late Variscan plutonic rocks from the External Crystalline Massifs of the Alps (France, Italy, Switzerland). J Petrology 40:1151–1185. https://doi.org/10.1093/petroj/40.7.1151
Debon F, Guerrot C, Ménot R-P (1998) Late Variscan granites of the Belledonne Massif (French Western Alps): an Early Visean magnesian plutonism. Schweiz Miner Petrogr Mitt 78:67–85. https://doi.org/10.5169/seals-59275
Debon F, Le Fort P (1988) A cationic classification of common plutonic rocks and their magmatic associations: principles, method, applications. Bulmi 111:493–510. https://doi.org/10.3406/bulmi.1988.8096
DePaolo DJ (1981) Trace element and isotopic effects of combined wallrock assimilation and fractional crystallization. Earth Planet Sci Lett 53:189–202. https://doi.org/10.1016/0012-821X(81)90153-9
Didier J, Duthou JL, Lameyre J (1982) Mantle and crustal granites: Genetic classification of orogenic granites and the nature of their enclaves. J Volcanol Geotherm Res 14:125–132
Dobmeier C, Pfeifer HR, Von Raumer JF (1999) The newly defined" Greenstone Unit"of the Aiguilles Rouges massif (western Alps): Remnant of an Early Palaeozoic oceanic island-arc? Schweiz Miner Petrogr Mitt 79:263–276
Downes H, Dupuy C, Leyreloup AF (1990) Crustal evolution of the Hercynian belt of Western Europe: Evidence from lower-crustal granulitic xenoliths (French Massif Central). Chem Geol 83:209–231. https://doi.org/10.1016/0009-2541(90)90281-B
Edel JB, Schulmann K, Lexa O, Lardeaux JM (2018) Late Palaeozoic palaeomagnetic and tectonic constraints for amalgamation of Pangea supercontinent in the European Variscan belt. Earth Sci Rev 177:589–612. https://doi.org/10.1016/j.earscirev.2017.12.007
Faure M, Lardeaux J-M, Ledru P (2009) A review of the pre-Permian geology of the Variscan French Massif Central. C R Geosci 341:202–213
Fernandez A, Guillot S, Ménot R-P, Ledru P (2002) Late Paleozoic polyphased tectonics in the SW Belledonne massif (external crystalline massifs, French Alps). Geodin Acta 15:127–139
Ferrando S, Lombardo B, Compagnoni R (2008) Metamorphic history of HP mafic granulites from the Gesso-Stura terrain (Argentera Massif, western Alps, Italy). Eur J Mineral 20:777–790
Finger F, Roberts MP, Haunschmid B, Schermaier A, Steyrer H-P (1997) Variscan granitoids of central Europe: their typology, potential sources and tectonothermal relations. Mineral Petrol 61(1–4):67–96
Foley SF, Venturelli G, Green DH, Toscani L (1987) The ultrapotassic rocks: Characteristics, classification, and constraints for petrogenetic models. Earth Sci Rev 24:81–134. https://doi.org/10.1016/0012-8252(87)90001-8
Franke W, Cocks LRM, Torsvik TH (2017) The Palaeozoic Variscan oceans revisited. Gondwana Res 48:257–284
Fréville K, Trap P, Faure M, Melleton J, Li X-H, Lin W, Blein O, Bruguier O, Poujol M (2018) Structural, metamorphic and geochronological insights on the Variscan evolution of the Alpine basement in the Belledonne Massif (France). Tectonophysics 726:14–42
Fréville K, Trap P, Vanardois J, Melleton J, Faure M, Bruguier O, Poujol M, Lach P (2022) Carboniferous-Permian tectono-metamorphic evolution of the Pelvoux Massif (External Crystalline Massif, Western Alps), with discussion on flow kinematics of

the Eastern-Variscan Shear Zone. Bull Soc Géol Fr 193:13. https://doi.org/10.1051/bsgf/2022008

Frost BR, Barnes CG, Collins WJ, Arculus RJ, Ellis DJ, Frost CD (2001) A geochemical classification for granitic rocks. J Petrol 42(11):2033–2048

Galli A, Le Bayon B, Schmidt MW, Burg J-P, Caddick MJ, Reusser E (2011) Granulites and charnockites of the Gruf Complex: Evidence for Permian ultra-high temperature metamorphism in the Central Alps. Lithos 124:17–45. https://doi.org/10.1016/j.lithos.2010.08.003

García-Arias M, Díez-Montes A, Villaseca C, Blanco-Quintero IF (2018) The Cambro-Ordovician Ollo de Sapo magmatism in the Iberian Massif and its Variscan evolution: A review. Earth Sci Rev 176:345–372. https://doi.org/10.1016/j.earscirev.2017.11.004

Gasquet D (1979) Etude pétrologique, géochimique et structurale des terrains cristallins de Belledonne et du Grand Chatelard traversés par les galeries E.D.F. Arc-Isère- Alpes Françaises. Doctoral dissertation, Université Scientifique et Médicale de Grenoble

Gaynor SP, Ruiz M, Schaltegger U (2022) The importance of high precision in the evaluation of U–Pb zircon age spectra. Chem Geol 603:120913. https://doi.org/10.1016/j.chemgeo.2022.120913

Giorgi L (1979) Contribution à l'étude géologique des terrains cristallins du Massif des Grandes Rousses . Isère- France - Alpes. Doctoral dissertation, Université Scientifique et Médicale de Grenoble

Grandjean V, Guillot S, Pecher A (1996) A new record of the LP-HT late-Variscan metamorphism: The Peyre-Arguet unit (Haut-Dauphine). C R Acad Sci II A 322:189–195

Griffin WL (2008) GLITTER: data reduction software for laser ablation ICP-MS. Laser Ablation ICP-MS in the Earth Sciences: Current practices and outstanding issues : 308–311

Guerrot C, Debon F (2000) U–Pb zircon dating of two contrasting Late Variscan plutonic suites from the Pelvoux massif (French Western Alps). Schweiz Miner Petrogr Mitt 80:249–256

Guillot S, Menot R (1999) Nappe stacking and first evidence of Late Variscan extension in the Belledonne Massif (External Crystalline Massifs, French Alps). Geodin Acta 12:97–111. https://doi.org/10.1016/S0985-3111(99)80026-6

Guillot S, Ménot R-P (2009) Paleozoic evolution of the External Crystalline Massifs of the Western Alps. C R Geosci 341:253–265. https://doi.org/10.1016/j.crte.2008.11.010

Guillot S, di Paola S, Ménot R-P, Ledru P, Spalla MI, Gosso G, Schwartz S (2009) Suture zones and importance of strike-slip faulting for Variscan geodynamic reconstructions of the External Crystalline Massifs of the western Alps. Bull Soc Géol Fr 180:483–500

Harlov DE, Austrheim H (2013) Metasomatism and the chemical transformation of rock: rock–mineral–fluid interaction in terrestrial and extraterrestrial environments. Metasomatism and the chemical transformation of rock. Springer, Berlin, pp 1–16

Hora JM, Tabaud A-S, Janoušek V, Erban Kochergina YV (2021) Potassic magmas of the Vosges Mts. (NE France) delimit the areal extent and nature of long-gone Variscan orogenic mantle domains. Lithos. https://doi.org/10.1016/j.lithos.2021.106304

Horstwood MSA, Košler J, Gehrels G, Jackson SE, McLean NM, Paton C, Pearson NJ, Sircombe K, Sylvester P, Vermeesch P, Bowring JF, Condon DJ, Schoene B (2016) Community-derived standards for LA–ICP–MS U–(Th–)Pb geochronology—uncertainty propagation, age interpretation and data reporting. Geostand Geoanal Res 40:311–332. https://doi.org/10.1111/j.1751-908X.2016.00379.x

Hoskin PWO, Schaltegger U (2003) The composition of zircon and igneous and metamorphic petrogenesis. Rev Mineral Geochem 53:27–62. https://doi.org/10.2113/0530027

Jackson SE, Pearson NJ, Griffin WL, Belousova EA (2004) The application of laser ablation-inductively coupled plasma–mass spectrometry to in situ U–Pb zircon geochronology. Chem Geol 211:47–69. https://doi.org/10.1016/j.chemgeo.2004.06.017

Jacob J-B, Guillot S, Rubatto D, Janots E, Melleton J, Faure M (2021a) Carboniferous high-P metamorphism and deformation in the Belledonne Massif (Western Alps). J Metamorph Geol 39:1009–1044. https://doi.org/10.1111/jmg.12600

Jacob J-B, Moyen J-F, Fiannacca P, Laurent O, Bachmann O, Janoušek V, Farina F, Villaros A (2021b) Crustal melting vs. fractionation of basaltic magmas: Part 2, Attempting to quantify mantle and crustal contributions in granitoids. Lithos. https://doi.org/10.1016/j.lithos.2021.106292

Jacob J-B, Janots E, Guillot S, Rubatto D, Fréville K, Melleton J, Faure M (2022) HT overprint of HP granulites in the Oisans-Pelvoux massif: Implications for the dynamics of the Variscan collision in the external western Alps. Lithos 416–417:106650. https://doi.org/10.1016/j.lithos.2022.106650

Jacob J-B, Janots E, Cordier C, Guillot S (2023) Discovery of Variscan orogenic peridotites in the Pelvoux Massif (Western Alps, France). Bull Soc Géol Fr 194:2. https://doi.org/10.1051/bsgf/2022021

Janoušek V, Holub FV (2007) The causal link between HP-HT metamorphism and ultrapotassic magmatism in collisional orogens: case study from the Moldanubian Zone of the Bohemian Massif. Proc Geol Assoc 118:75–86. https://doi.org/10.1016/S0016-7878(07)80049-6

Janoušek V, Wiegand BA, Žák J (2010) Dating the onset of Variscan crustal exhumation in the core of the Bohemian Massif: new U–Pb single zircon ages from the high-K calc-alkaline granodiorites of the Blatná suite, Central Bohemian Plutonic Complex. JGS 167:347–360. https://doi.org/10.1144/0016-76492009-008

Janoušek V, Aichler J, Hanžl P, Gerdes A, Erban V, Žáček V, Pecina V, Pudilová M, Hrdličková K, Mixa P, Žáčková E (2014) Constraining genesis and geotectonic setting of metavolcanic complexes: a multidisciplinary study of the Devonian Vrbno Group (Hrubý Jeseník Mts., Czech Republic). Int J Earth Sci 103:455–483. https://doi.org/10.1007/s00531-013-0975-4

Janoušek V, Bonin B, Collins WJ, Farina F, Bowden P (2019) Post-Archean granitic rocks: contrasting petrogenetic processes and tectonic environments. Geol Soc Lond Spec Public 491:1–8

Janoušek V, Hanžl P, Svojtka M, Hora JM, Kochergina YVE, Gadas P, Holub FV, Gerdes A, Verner K, Hrdličková K, Daly JS, Buriánek D (2020) Ultrapotassic magmatism in the heyday of the Variscan Orogeny: the story of the Třebíč Pluton, the largest durbachitic body in the Bohemian Massif. Int J Earth Sci 109:1767–1810. https://doi.org/10.1007/s00531-020-01872-2

Janoušek V, Erban Kochergina YV, Andronikov AV, Kusbach VK (2022) Decoupling of Mg from Sr–Nd isotopic compositions in Variscan subduction-related plutonic rocks from the Bohemian Massif: implications for mantle enrichment processes and genesis of orogenic ultrapotassic magmatic rocks. Int J Earth Sci 111:1491–1518. https://doi.org/10.1007/s00531-022-02199-w

Kunz BE, Manzotti P, von Niederhäusern B, Engi M, Darling JR, Giuntoli F, Lanari P (2018) Permian high-temperature metamorphism in the Western Alps (NW Italy). Int J Earth Sci 107:203–229. https://doi.org/10.1007/s00531-017-1485-6

Lardeaux JM, Schulmann K, Faure M, Janoušek V, Lexa O, Skrzypek E, Edel JB, Štípská P (2014) The moldanubian zone in the French Massif Central, Vosges/Schwarzwald and Bohemian Massif revisited: differences and similarities. Geol Soc Lond Spec Public 405:7–44

Laurent JC (1992) Les épisodes magmatiques filoniens basiques du Massif des Ecrins-Pelvoux entre Carbonifère et Lias. Doctoral dissertation, Université Joseph-Fourier-Grenoble I

Laurent O, Couzinié S, Zeh A, Vanderhaeghe O, Moyen J-F, Villaros A, Gardien V, Chelle-Michou C (2017) Protracted, coeval crust and mantle melting during Variscan late-orogenic evolution: U–Pb dating in the eastern French Massif Central. Int J Earth Sci 106:421–451. https://doi.org/10.1007/s00531-016-1434-9

Le Fort P (1971) Géologie du Haut-Dauphiné cristallin (Alpes Française): Etudes pétrologique et structurale de la partie occidentale. Doctoral dissertartion, Université Nancy I

Ledru P, Courrioux G, Dallain C, Lardeaux JM, Montel JM, Vanderhaeghe O, Vitel G (2001) The Velay dome (French Massif Central): melt generation and granite emplacement during orogenic evolution. Tectonophysics 342:207–237. https://doi.org/10.1016/S0040-1951(01)00165-2

Linnemann U, Gerdes A, Hofmann M, Marko L (2014) The Cadomian Orogen: Neoproterozoic to Early Cambrian crustal growth and orogenic zoning along the periphery of the West African Craton—Constraints from U–Pb zircon ages and Hf isotopes (Schwarzburg Antiform, Germany). Precambr Res 244:236–278. https://doi.org/10.1016/j.precamres.2013.08.007

Linnen RL, Keppler H (1997) Columbite solubility in granitic melts: consequences for the enrichment and fractionation of Nb and Ta in the Earth's crust. Contrib Mineral Petrol 128:213–227. https://doi.org/10.1007/s004100050304

Luais B, Telouk P, Albaréde F (1997) Precise and accurate neodymium isotopic measurements by plasma-source mass spectrometry. Geochim Cosmochim Acta 61:4847–4854

Ludwig KR (2003) User's manual for IsoPlot 3.0. A geochronological toolkit for Microsoft Excel 71

Lugmair GW, Marti K (1978) Lunar initial 143Nd/144Nd: differential evolution of the lunar crust and mantle. Earth Planet Sci Lett 39:349–357

Maierová P, Schulmann K, Štípská P, Gerya T, Lexa O (2021) Translithospheric diapirism explains the presence of ultra-high pressure rocks in the European Variscides. Commun Earth Environ 2:56. https://doi.org/10.1038/s43247-021-00122-w

Manzotti P, Ballèvre M, Poujol M (2016) Detrital zircon geochronology in the Dora-Maira and Zone Houillère: a record of sediment travel paths in the Carboniferous. Terra Nova 28:279–288. https://doi.org/10.1111/ter.12219

Martínez Catalán JR, Schulmann K, Ghienne J-F (2021) The Mid-Variscan Allochthon: Keys from correlation, partial retrodeformation and plate-tectonic reconstruction to unlock the geometry of a non-cylindrical belt. Earth Sci Rev 220:103700. https://doi.org/10.1016/j.earscirev.2021.103700

Medaris G, Ackerman L, Jelínek E, Michels ZD, Erban V, Kotková J (2015) Depletion, cryptic metasomatism, and modal metasomatism (refertilization) of Variscan lithospheric mantle: evidence from major elements, trace elements, and Sr–Nd–Os isotopes in a Saxothuringian garnet peridotite. Lithos 226:81–97. https://doi.org/10.1016/j.lithos.2014.10.007

Melleton J, Cocherie A, Faure M, Rossi P (2010) Precambrian protoliths and Early Paleozoic magmatism in the French Massif Central: U–Pb data and the North Gondwana connection in the west European Variscan belt. Gondwana Res 17:13–25. https://doi.org/10.1016/j.gr.2009.05.007

Ménot R-P (1986) Les formations plutono-volcaniques dévoniennes de Rioupéroux-Livet (Massifs cristallins externes des Alpes Françaises): nouvelles définitions lithostratigraphique et pétrographique. Schweiz Mineral Petrogr Mitt 66:229–258

Ménot R-P (1987) Magmatismes et structuration orogénique paléozoiques de la chaine de Belledonne (Massifs cristallins externes alpins). Le domaine sud—occidental. Géol Alpine 63:55–93

Ménot RP (1988) An overview of the geology of the Belledonne massif (external crystalline massifs of Western Alps). Schweiz Mineral Petrogr Mitt 70:33–53

Ménot R-P, Bonhomme MG, Vivier G (1987) Structuration tectonométamorphique carbonifère dans le massif de Belledonne (Alpes Occidentales françaises), apport de la géochronologie K/Ar des amphiboles. Schweiz Miner Petrogr Mitt 67:273–284

Ménot RP, Paquette JL (1993) Geodynamic significance of basic and bimodal magmatism in the external domain. In: Pre-mesozoic geology in the Alps. Springer, Berlin, pp 241–254

Moyen J-F (2009) High Sr/Y and La/Yb ratios: the meaning of the "adakitic signature." Lithos 112(3–4):556–574

Moyen J-F, Laurent O, Chelle-Michou C, Couzinié S, Vanderhaeghe O, Zeh A, Villaros A, Gardien V (2017) Collision vs. subduction-related magmatism: two contrasting ways of granite formation and implications for crustal growth. Lithos 277:154–177. https://doi.org/10.1016/j.lithos.2016.09.018

Moyen J-F, Janoušek V, Laurent O, Bachmann O, Jacob J-B, Farina F, Fiannacca P, Villaros A (2021) Crustal melting vs. fractionation of basaltic magmas: Part 1, granites and paradigms. Lithos 402–403:106291. https://doi.org/10.1016/j.lithos.2021.106291

Negga HS (1984) Comportement de l'uranium lors des métamorphismes tardi-hercinien et alpin dans les massifs des Aiguilles rouges et de Belledone (Vallorcine, Lauzière). Alpes occidentales. Doctoral dissertation, Université de Lorraine

Oliver RA (1994) Géologie et géochimie des granitoides et des roches basique associées du Valsenestre : place dans la province magmatique varisque des massifs cristallins externes du Haut Dauphiné (Alpes occidentales françaises). Doctoral dissertation, Université Joseph-Fourier - Grenoble I

Paquette JL, Menot RP, Peucat JJ (1989) REE, Sm-Nd and U–Pb zircon study of eclogites from the Alpine External Massifs (Western Alps): evidence for crustal contamination. Earth Planet Sci Lett 96:181–198

Parrish RR, Parrish RR, Noble SR (2003) Zircon U–Th–Pb geochronology by isotope dilution—thermal ionization mass spectrometry (ID-TIMS). Rev Mineral Geochem 53:183–213

Paton C, Hellstrom J, Paul B, Woodhead J, Hergt J (2011) Iolite: Freeware for the visualisation and processing of mass spectrometric data. J Anal at Spectrom 26:2508–2518. https://doi.org/10.1039/C1JA10172B

Peccerillo A, Taylor SR (1976) Geochemistry of eocene calc-alkaline volcanic rocks from the Kastamonu area, Northern Turkey. Contrib Mineral Petrol 58:63–81. https://doi.org/10.1007/BF00384745

Pecher A (1970) Etude pétrographique de la partie orientale du massif des Ecrins-Pelvoux: le socle ancien - Alpes françaises. Doctoral dissertation, Université Scientifique et Médicale de Grenoble

Pin C, Paquette J-L (1997) A mantle-derived bimodal suite in the Hercynian Belt: Nd isotope and trace element evidence for a subduction-related rift origin of the Late Devonian Brévenne metavolcanics, Massif Central (France). Contrib Mineral Petrol 129:222–238. https://doi.org/10.1007/s004100050334

Pin C, Zalduegui JS (1997) Sequential separation of light rare-earth elements, thorium and uranium by miniaturized extraction chromatography: application to isotopic analyses of silicate rocks. Anal Chim Acta 339:79–89

Pitcher WS (1987) Granites and yet more granites forty years on. Geol Rundsch 76:51–79. https://doi.org/10.1007/BF01820573

Poncerry E (1981) Contribution à l'étude géologique des granitoïdes de Vallorcine, Beaufort, Lauzière, de leur encaissant et des minéralisations uranifères associées. Alpes Françaises. Doctoral dissertation, Université Scientifique et Médicale de Grenoble

Profeta L, Ducea MN, Chapman JB, Paterson SR, Gonzales SMH, Kirsch M, Petrescu L, DeCelles PG (2015) Quantifying crustal thickness over time in magmatic arcs. Sci Rep 5:17786. https://doi.org/10.1038/srep17786

Rossi P, Cocherie A (1991) Genesis of a Variscan batholith: Field, petrological and mineralogical evidence from the Corsica-Sardinia

Batholith. Tectonophysics 195:319–346. https://doi.org/10.1016/0040-1951(91)90219-I

Rubatto D, Ferrando S, Compagnoni R, Lombardo B (2010) Carboniferous high-pressure metamorphism of Ordovician protoliths in the Argentera Massif (Italy), Southern European Variscan belt. Lithos 116:65–76

Ruiz M, Schaltegger U, Gaynor SP, Chiaradia M, Abrecht J, Gisler C, Giovanoli F, Wiederkehr M (2022) Reassessing the intrusive tempo and magma genesis of the late Variscan Aar batholith: U–Pb geochronology, trace element and initial Hf isotope composition of zircon. Swiss J Geosci 115:20. https://doi.org/10.1186/s00015-022-00420-1

Salters VJM, Stracke A (2004) Composition of the depleted mantle. Geochem Geophys Geosyst. https://doi.org/10.1029/2003GC000597

Scambelluri M, Hermann J, Morten L, Rampone E (2006) Melt- versus fluid-induced metasomatism in spinel to garnet wedge peridotites (Ulten Zone, Eastern Italian Alps): clues from trace element and Li abundances. Contrib Mineral Petrol 151:372–394. https://doi.org/10.1007/s00410-006-0064-9

Schaltegger U (1997) Magma pulses in the Central Variscan Belt: episodic melt generation and emplacement during lithospheric thinning. Terra Nova 9:242–245. https://doi.org/10.1111/j.1365-3121.1997.tb00021.x

Schaltegger U, Davies JHFL (2017) Petrochronology of zircon and baddeleyite in igneous rocks: reconstructing magmatic processes at high temporal resolution. Rev Mineral Geochem 83:297–328. https://doi.org/10.2138/rmg.2017.83.10

Schaltegger U, Abrecht J, Corfu F (2003) The Ordovician orogeny in the Alpine basement: constraints from geochronology and geochemistry in the Aar Massif (Central Alps). Swiss Bull Mineral Petrol 83:183–239

Schaltegger U, Nowak A, Ulianov A, Fisher CM, Gerdes A, Spikings R, Whitehouse MJ, Bindeman I, Hanchar JM, Duff J, Vervoort JD, Sheldrake T, Caricchi L, Brack P, Müntener O (2019) Zircon Petrochronology and 40Ar/39Ar Thermochronology of the Adamello Intrusive Suite, N. Italy: Monitoring the Growth and Decay of an Incrementally Assembled Magmatic System. J Petrol 60:701–722. https://doi.org/10.1093/petrology/egz010

Schulmann K, Konopásek J, Janoušek V, Lexa O, Lardeaux J-M, Edel J-B, Štípská P, Ulrich S (2009) An Andean type Palaeozoic convergence in the Bohemian Massif. C R Geosci 341:266–286. https://doi.org/10.1016/j.crte.2008.12.006

Schulmann K, Catalán J-RM, Lardeaux J-M, Janoušek V, Oggiano G (2014) The Variscan orogeny: extent, timescale and the formation of the European crust. Geol Soc Lond Spec Public 405:1–6. https://doi.org/10.1144/SP405.15

Schuster R, Stüwe K (2008) Permian metamorphic event in the Alps. Geology 36:603–606. https://doi.org/10.1130/G24703A.1

Simeon Y (1979) Etude pétrologique, géochimique et structurale des terrains cristallins de Belledonne entre l'Arc et l'Isère (Alpes françaises). Doctoral dissertation, Université Scientifique et Médicale de Grenoble

Simien F, Mattauer M, Allègre CJ (1999) Nd Isotopes in the Stratigraphic Record of the Montagne Noire (French Massif Central): no significant paleozoic Juvenile Inputs, and Pre-Hercynian Paleogeography. J Geol 107:87–97. https://doi.org/10.1086/314332

Simonetti M, Carosi R, Montomoli C, Langone A, D'Addario E, Mammoliti E (2018) Kinematic and geochronological constraints on shear deformation in the Ferriere-Mollières shear zone (Argentera-Mercantour Massif, Western Alps): implications for the evolution of the Southern European Variscan Belt. Int J Earth Sci 107:2163–2189. https://doi.org/10.1007/s00531-018-1593-y

Simonetti M, Carosi R, Montomoli C, Cottle JM, Law RD (2020) Transpressive Deformation in the Southern European Variscan Belt: New Insights From the Aiguilles Rouges Massif (Western Alps). Tectonics 39:e2020TC006153. https://doi.org/10.1029/2020TC006153

Skrzypek E, Tabaud A-S, Edel J-B, Schulmann K, Cocherie A, Guerrot C, Rossi P (2012) The significance of Late Devonian ophiolites in the Variscan orogen: a record from the Vosges Klippen Belt. Int J Earth Sci (geol Rundsch) 101:951–972. https://doi.org/10.1007/s00531-011-0709-4

Sláma J, Košler J, Condon DJ, Crowley JL, Gerdes A, Hanchar JM, Horstwood MSA, Morris GA, Nasdala L, Norberg N, Schaltegger U, Schoene B, Tubrett MN, Whitehouse MJ (2008) Plešovice zircon—a new natural reference material for U–Pb and Hf isotopic microanalysis. Chem Geol 249:1–35. https://doi.org/10.1016/j.chemgeo.2007.11.005

Soder CG, Romer RL (2018) Post-collisional potassic-ultrapotassic magmatism of the variscan orogen: implications for mantle metasomatism during continental subduction. J Petrol 59:1007–1034. https://doi.org/10.1093/petrology/egy053

Soejono I, Machek M, Sláma J, Janoušek V, Kohút M (2020) Cambro-Ordovician anatexis and magmatic recycling at the thinned Gondwana margin: new constraints from the Kouřim Unit, Bohemian Massif. J Geol Soc 177:325–341. https://doi.org/10.1144/jgs2019-037

Steiger RH, Jäger E (1977) Subcommission on geochronology: Convention on the use of decay constants in geo- and cosmochronology. Earth Planet Sci Lett 36:359–362. https://doi.org/10.1016/0012-821X(77)90060-7

Stephan T, Kroner U, Romer RL (2019) The pre-orogenic detrital zircon record of the Peri-Gondwanan crust. Geol Mag 156:281–307. https://doi.org/10.1017/S0016756818000031

Storck J-C, Laurent O, Karakas O, Wotzlaw J-F, Galli A, Sinigoi S, Bachmann O, Chelle-Michou C (2021) Mantle versus crustal contributions in crustal-scale magmatic systems (Sesia Magmatic System, northern Italy) from coupling Hf isotopes and numerical modelling. Contrib Mineral Petrol 176(11):95. https://doi.org/10.1007/s00410-021-01847-9

Strzerzynski P, Guillot S, Courrioux G, Ledru P (2005) Modélisation géométrique 3D des granites stéphaniens du massif du Pelvoux (Alpes, France). C R Geosci 337:1284–1292

Sun S-S, McDonough WF (1989) Chemical and isotopic systematics of oceanic basalts: implications for mantle composition and processes. Geol Soc Lond Spec Public 42:313–345

Sundell K, Laskowski A, Kapp P, Ducea M, Chapman J (2021) Jurassic to neogene quantitative crustal thickness estimates in southern tibet. GSAT 31:4–10. https://doi.org/10.1130/GSATG461A.1

Tabaud A-S, Janoušek V, Skrzypek E, Schulmann K, Rossi P, Whitechurch H, Guerrot C, Paquette J-L (2015) Chronology, petrogenesis and heat sources for successive Carboniferous magmatic events in the Southern-Central Variscan Vosges Mts (NE France). J Geol Soc London 172:87–102

Tanaka T, Togashi S, Kamioka H, Amakawa H, Kagami H, Hamamoto T, Yuhara M, Orihashi Y, Yoneda S, Shimizu H (2000) JNdi-1: a neodymium isotopic reference in consistency with LaJolla neodymium. Chem Geol 168(3–4):279–281

Teyssier C, Whitney DL (2002) Gneiss domes and orogeny. Geology 30:1139–1142

Vanardois J, Lahfid A, Trap P, Lacroix B, Roger F, Guillou-Frottier L, Marquer D, Paquette J-L, Melleton J (2022a) Thermal evolution of a Variscan syn-orogenic intracontinental basin (Servoz basin, Western Alps): RSCM geothermometry and geochronology. Swiss J Geosci 115:23. https://doi.org/10.1186/s00015-022-00423-y

Vanardois J, Roger F, Trap P, Goncalves P, Lanari P, Paquette J-L, Marquer D, Cagnard F, Le Bayon B, Melleton J (2022b) Exhumation of deep continental crust in a transpressive regime: the example

of Variscan eclogites from the Aiguilles-Rouges Massif (Western Alps). J Metamorph Geol 2022:1

Vanardois J, Trap P, Roger F, Melleton J, Marquer D, Paquette J-L, Goncalves P, Cagnard F, Le Bayon B (2022c) Deformation, crustal melting and magmatism in the crustal-scale East-Variscan Shear Zone (Aiguilles-Rouges and Mont-Blanc massifs, Western Alps). J Struct Geol 163:104724. https://doi.org/10.1016/j.jsg.2022.104724

Vanderhaeghe O, Laurent O, Gardien V, Moyen J-F, Gébelin A, Chelle-Michou C, Couzinié S, Villaros A, Bellanger M (2020) Flow of partially molten crust controlling construction, growth and collapse of the Variscan orogenic belt: the geologic record of the French Massif Central. Bull Soc Géol Fr. https://doi.org/10.1051/bsgf/2020013

Verjat JL (1981) Etude pétrologique et structurale des terrains cristallins du sud-est de Belledonne, à l'ouest du col du Glandon - Alpes françaises. Doctoral dissertation, Université Scientifique et Médicalse de Grenoble

Vermeesch P (2012) On the visualisation of detrital age distributions. Chem Geol 312–313:190–194. https://doi.org/10.1016/j.chemgeo.2012.04.021

Vermeesch P (2018) Statistical models for point-counting data. Earth Planet Sci Lett 501:112–118

Vivier G, Ménot R-P, Giraud P (1987) Magmatismes et structuration orogénique Paléozoiques de la chaine de Belledonne (Massifs cristallins externes alpins). Le Domaine Nord Orient Géol Alpine (grenoble) 63:25–53

Von Raumer JF, Stampfli GM (2008) The birth of the Rheic Ocean—Early Palaeozoic subsidence patterns and subsequent tectonic plate scenarios. Tectonophysics 461(1–4):9–20

Von Raumer JF, Finger F, Veselá P, Stampfli GM (2014) Durbachites–Vaugnerites—a geodynamic marker in the central European Variscan orogen. Terra Nova 26:85–95

Von Raumer JF, Stampfli GM, Arenas R, Martínez SS (2015) Ediacaran to Cambrian oceanic rocks of the Gondwana margin and their tectonic interpretation. Int J Earth Sci 104:1107–1121

Von Raumer JF, Bussy F (2004) Mont Blanc and Aiguilles Rouges geology of their polymetamorphic basement (external massifs, Westerns Alps, France-Switzerland). In: Mémoires de Géologie (Lausanne), pp 1–210

Wiedenbeck M, Allé P, Corfu F, Griffin WL, Meier M, Oberli F, Quadt AV, Roddick JC, Spiegel W (1995) Three Natural Zircon Standards for U–Th–Pb, Lu–Hf, Trace element and ree analyses. Geostand Newsl 19:1–23. https://doi.org/10.1111/j.1751-908X.1995.tb00147.x

Žák J, Verner K, Janoušek V, Holub FV, Kachlík V, Finger F, Hajná J, Tomek F, Vondrovic L, Trubač J (2014) A plate-kinematic model for the assembly of the Bohemian Massif constrained by structural relationships around granitoid plutons. Geol Soc Spec Publ 405:169–196. https://doi.org/10.1144/SP405.9